NONLINEAR AND QUANTUM OPTICS IN FEW-MODE-FIBERS

by

AFSHIN SHAMSSHOOLI

DISSERTATION

Submitted in partial fulfillment of the requirements
for the degree of Doctor of Philosophy at
The University of Texas at Arlington
May 2021

Arlington, Texas

Supervising Committee:

Michael Vasilyev, Supervising Professor
Robert Magnusson
Kambiz Alavi
Weidong Zhou
Alice Sun

Acknowledgements

First and foremost, I would like to thank my supervisor Prof. Michael Vasilyev from bottom of my heart who provided me such a unique opportunity of working with him in Nonlinear Optics and Nanophotonics Laboratory of University of Texas at Arlington. I am so grateful to him for his invaluable guidance, continuous support, and patience during my PhD study. His immense knowledge and deep insight have encouraged me in all the time of my academic research and daily life. His brilliant ideas have always been taking me out from my research problems and helping me to solve them. I am truly honored working under his supervision.

I also want to thank Prof. Robert Magnusson, Prof. Kambiz Alavi, Prof. Weidong Zhou, and Prof. Alice Sun for their kind consent to be on my PhD supervising committee. Beside being on my supervising committee, I have known them for almost 5 years. I have learned so many things from them.

I also would like to extend my gratitude to all my lab group members- Cheng Guo, Dr. Subrata Das, Kamanashis Saha, Nirjhor Tahmidur Rouf, Dr. Young B. Kwon, Dr. Lu Li and Dr. Sarath Samudrala for making our group intimate and collaborative environment where we worked together happily.

Thanks to Dr. Nader Hozhabri and all Nanofab people, Huan Nguyen, Dennis Bueno and Kevin Chambers for their constant help and support all these years.

I would like to acknowledge the funding agencies- National Science Foundation for funding my project, and our research collaborator, Dr. Francesca Parmigiani, from Microsoft Research for providing a few-mode fiber which made this project feasible. I am also thankful to

the Dept. of Electrical Engineering, UTA and Shimadzu Institute- Nanotechnology Research Center for giving me the opportunity to conduct my research work.

Finally, MY FAMILY. I must thank my lovely wife, Sheida, for always being alongside me during good and bad days. She has not been just the love of my life; she has always been my true friend that I am blessed by. Without her tremendous understanding and encouragement in the past few years, it would be impossible for me to complete my study. I never got an opportunity to thank my parents. They have always been there to help and encourage me. Thank You Dear Parents. I also want to thank my siblings, Farshad and Farnoosh, for being a big support for me throughout my life. And I am very thankful to my parents-in-law who supported Sheida and I endlessly.

ABSTRACT

Nonlinear And Quantum Optics In Few-Mode-Fibers

Afshin Shamsshooli, Ph.D.

The University of Texas at Arlington, 2021

Supervising Professor: Michael Vasilyev

In the absence of quantum repeaters, fiber loss sets the hard limit on secure quantum communication rate. Single-photon source rate decays exponentially with the length of fiber. The only way to scale the rate up is by increasing the number of modes over which the single-photon or entangled states are transmitted, for subsequent use in. quantum communication, computing, or information processing. Entanglement in multiple degrees of freedom, e.g., in polarization, frequency, time-bin, and spatial modes has a potential for carrying larger amounts of quantum information. In this project, we explore spatial modes in the few-mode fiber for generation and processing of spatially-entangled states. There are 2 requirements to use spatial-mode entanglement in quantum communication: 1) Generation of spatially-entangled states, and 2) Mode-selective frequency conversion, which could make alternating projective measurements in mutually unbiased bases (these projective measurements make it possible to decode the information encoded in spatial entanglement). In this thesis, both of these 2 requirements have been addressed via inter-mode four-wave mixing (IM-FWM) in a few-mode fiber.

In the first part of the work, two IM-FWM processes necessary for mode-selective frequency conversion have been implemented, and upconversion of any combination of two signal modes from C-band to fundamental mode in S-band with crosstalk below –20 dB has been

experimentally demonstrated. These experiments have been realized in two different mode spaces: one in (LP_{01}, LP_{11a}) mode space, and the other in (LP_{11a}, LP_{11b}) mode space compatible with Orbital-Angular-Momentum (OAM) encoding.

In the second part of the work, in the effort to generate spatially-entangled photon pairs, a combination of two IM-FWM processes that couples an arbitrary two-mode signal combination to an orthogonal idler mode has been demonstrated in a few-mode fiber. When both processes have been combined, it was observed that they couple the input two-mode classical seed signal to an orthogonal two-mode idler for various signal-mode superpositions. This mode anticorrelation between the generated signal and idler beams has been experimentally demonstrated for (LP_{01}, LP_{11a}). We have also demonstrated the coupling between the signal and idler beams in the orthogonal modes of (LP_{11a}, LP_{11b}) mode space, promising the generation of OAM-entangled pairs directly in the few-mode fiber.

Contents

List of Figures

Chapter 1: Introduction

In the absence of quantum repeaters, fiber loss sets the hard limit on quantum communication rate. Single-photon source rate decays exponentially with respect to the length of fiber. The only way to scale the rate up is by increasing the number of modes such as WDM / frequency / temporal modes, polarization modes, and spatial modes. Entangled states are essential for quantum communication, computing, and information processing. Entanglement in multiple degrees of freedom, e.g., in polarization, frequency, time-bin, and spatial modes has a potential for carrying larger amounts of quantum information, which is important for quantum communication and information processing. There are 2 requirements to use spatial-mode entanglement in quantum communication: 1) Mode-selective frequency conversion which could enable us to make alternating projective measurements in mutually unbiased bases (these projective measurements make us able to decode spatially-entangled encoded information) 2) Generation of spatially-entangled states.

Mode-selective frequency conversion is an important tool for mode-division multiplexing optical communication links. Mode-division multiplexing promises increase in channel capacity of both classical and quantum communications [1, 2], hereby bringing attention to multiplexers and demultiplexers of spatial modes. One of desired features of the mode demultiplexer is dynamic reconfigurability of its mode basis. In classical transmission, such reconfiguration could reverse the mode mixing and relax the requirements on electronic processing of the received signals. In quantum key distribution, switching between mutually unbiased mode bases could increase the dimension of the Hilbert space used for encoding [3]. In either case, low loss and low crosstalk of the demultiplexer are important. Not long ago, our research group has demonstrated such a

demultiplexer in a two-mode $LiNbO_3$ waveguide [4, 5], where, by adjusting the spatial profile of a 1560-nm pump wave, one could selectively upconvert either mode TM_{00}, or mode TM_{01}, or any superposition of these two modes of a 1540-nm signal to TM_{01} mode at 775 nm, for both classical [4] and single-photon-level [5] signals. Compared to $LiNbO_3$ platform, nonlinear few-mode fibers (FMF) can offer wider design options for mode- and dispersion-engineering and better mode match to the FMFs used in transmission links [6-8]. Therefore, we decided to use this platform and realize mode-selective frequency conversion. In the first part of this dissertation, we propose a scheme of similar functionality (mode demultiplexing by mode-selective frequency conversion) in a $\chi^{(3)}$ nonlinear medium, such as FMF, based on a combination of two inter-modal four-wave mixing (IM-FWM) processes.

In addition to this application, IM-FWM in FMF has recently attracted attention for tunable and broadband wavelength conversion [6, 9-12]. IM-FWM in a few-mode fiber has been used for frequency conversion of one out of many wavelength-division multiplexing (WDM) channels on 100-GHz grid with channel selectivity better than 16 dB [10]. IM-FWM-based simultaneous wavelength conversion of many WDM channels encoded with advanced modulation formats has also been demonstrated [11, 12]. The emergence of nonlinear few-mode fibers with very close values of group velocity dispersion in all modes makes them a promising platform for inter-modal nonlinear-optical signal processing [13]. Realization of mode-selective frequency conversion would enable dynamically reconfigurable mode-division multiplexing. In mode-selective frequency conversion project in this dissertation, we show good crosstalk performance (mode selectivity) for each of the two involved IM-FWM processes individually. Then, we implement both of these two processes simultaneously and demonstrate their combined ability to handle any mode superposition in the two-mode (LP_{01}, LP_{11a}) signal space.

As mentioned above, the second requirement to use spatial-mode entanglement in quantum communication is generation of spatially-entangled states. While polarization, frequency, and time-bin entanglement generation has already been implemented in integrated form compatible with low-loss transport over optical fiber, the spatial entanglement still relies on bulk-crystal-based setups [14]. The spatially- or orbital-angular-momentum- (OAM) entangled photons have been generated in crystal platforms and transported over various media: turbulent free-space [15], hollow-core photonic crystal fiber [16], a few-mode fiber (FMF) [17-19] , and vortex fiber [20]. As a possible alternative to crystal platform, IM-FWM in FMF is gaining traction for making nonlinear devices, owing to FMF's wide options for mode- and dispersion-engineering, and excellent mode match to the FMFs used in low-loss transmission links [6-8]. Furthermore, IM-FWM in FMFs could potentially interface optical quantum states with quantum-state signal processing devices [21]. Correlated photon pairs [22-24] and hybrid entanglement between frequency and spatial modes [25] were recently generated in FMFs by IM-FWM, but no attempts of generating spatial-mode entanglement through IM-FWM have been reported yet.

In this regard, in the second part of this dissertation, we introduce a novel scheme for generation of spatial-mode-entangled photon pairs directly in the FMF using a combination of two IM-FWM processes. Using classical seed signals, we experimentally measure signal-idler mode selectivity separately for these two processes. In the next development, we further combine both processes together and observe that they couple the input two-mode seed signal to an orthogonal two-mode idler for various signal-mode superpositions.

After having implemented both mode-selective frequency conversion and mode-selective signal-idler generation in the space of LP_{01} and LP_{11a} modes, in the third part of this dissertation, we describe OAM-compatible mode-selective frequency conversion in a few-mode fiber and

experimentally demonstrate downconversion of various superpositions of signal modes in (LP_{11a}, LP_{11b}) mode space. Afterwards, we describe a novel scheme for generation of OAM-entangled photons in a few-mode fiber.

Chapter 2: Theory of four-wave mixing in few-mode fibers

In this chapter, we explain the theory of four-wave mixing in few-mode fibers and derive the phase-matching condition for it. We introduce a fiber which supports 3 non-degenerate spatial modes and measure its dispersion for each individual mode. Afterwards, we describe 2 novel schemes: first for mode-selective frequency conversion in a few-mode fiber and second one for spatial-mode entanglement in a few-mode fiber.

2.1 Four-wave mixing in few-mode fibers

Four-wave mixing (FWM) is a third-order process involving up to three optical waves with different frequencies to generate a fourth wave through the third-order nonlinearity. General case for FWM is shown in Figure 1 where ω is the optical angular frequency for each wave [26]. The idler wave is generated at a frequency ω_4, which is determined by the energy conservation relation:

$$\omega_4 = \omega_2 + \omega_3 - \omega_1 \tag{2.1}$$

Following phase-matching (PM) condition also needs to be satisfied:

$$\beta(\omega_4) = \beta(\omega_2) + \beta(\omega_3) - \beta(\omega_1) \tag{2.2}$$

β is the propagation constant for each wave.

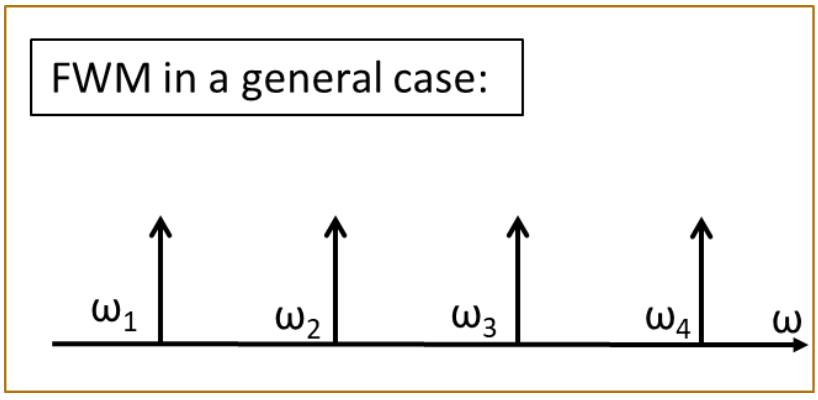

Figure 1. General case of four-wave mixing.

PM condition in bulk nonlinear-optical materials is done by tuning the angle (wavevector); analogous functionality can be realized in fiber with higher-order modes, as can be seen in Figure 2.

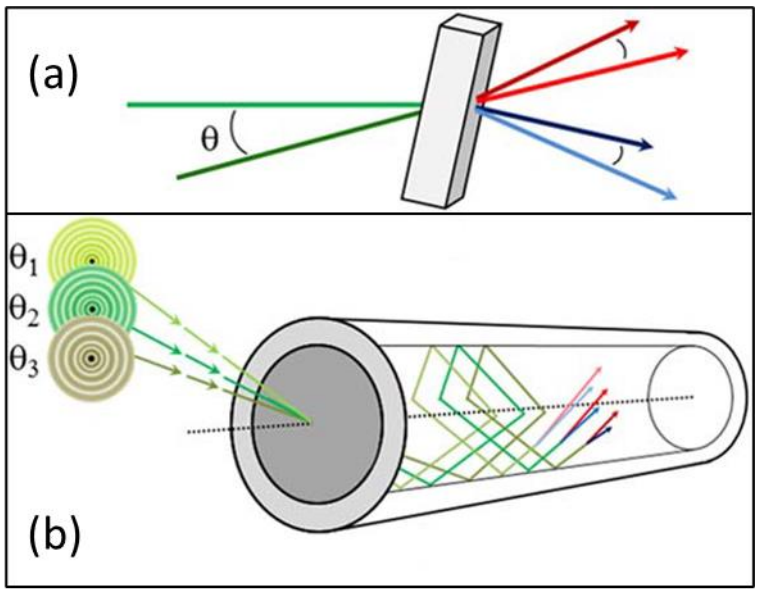

Figure 2. (a) PM in bulk material by angle tuning, (b) PM in multimode fiber by launching higher order modes.

For an efficient IM-FWM in FMFs, phase-matching condition would be as follows [27]:

$$\Delta\beta = \beta^{(l)}(\omega_i) - \beta^{(m)}(\omega_j) + \beta^{(n)}(\omega_k) - \beta^{(o)}(\omega_l) \approx 0 \qquad (2.3)$$

where the indices *i,j,k,l* label the waves and $\beta^{(r)}(\omega_q)$ is the propagation constant of the q^{th} wave propagating in the r^{th} fiber mode. In practice, the frequencies of the four waves participating in the FWM process are close enough to each other (typical optical frequencies in FWM for telecom wavelength are around 193 THz, whereas their differences are in order of few THz) which gives the opportunity to expand all propagation constants in a Taylor series around a common reference frequency ω_0, often chosen somewhere near the middle of the frequency range involved. For a given mode *r*, expansion to third order provides [28]:

$$\beta^{(r)}(\omega)=\beta_0^{(r)}+\beta_1^{(r)}\Delta\omega+\frac{\beta_2^{(r)}}{2}(\Delta\omega)^2+\frac{\beta_3^{(r)}}{6}(\Delta\omega)^3+\ldots, \qquad (2.4)$$

where $\Delta\omega = \omega-\omega_0$ and $\beta_0^{(r)} = \beta_0^{(r)}(\omega_0)$. The first, second, and third derivatives of β are β_1, β_2, and β_3, representing the inverse of the group velocity, its dispersion, and third-order dispersion evaluated at ω_0, respectively [27]. For a single-mode fiber (SMF), all waves involved in the FWM process propagate in the same spatial mode (fundamental mode). Therefore, they have the same values of β_n to all orders of Taylor's expansion. One can easily prove that $\Delta\beta=0$ cannot be satisfied in SMFs for any non-degenerate FWM process at reasonable powers unless one operates at wavelengths near the zero group-velocity dispersion ($\beta_2=0$). FWM in SMFs usually requires other techniques to realize phase matching, such as the use of nonlinear phase shifts obtained with very high power [29], or the use of birefringent fibers [30].

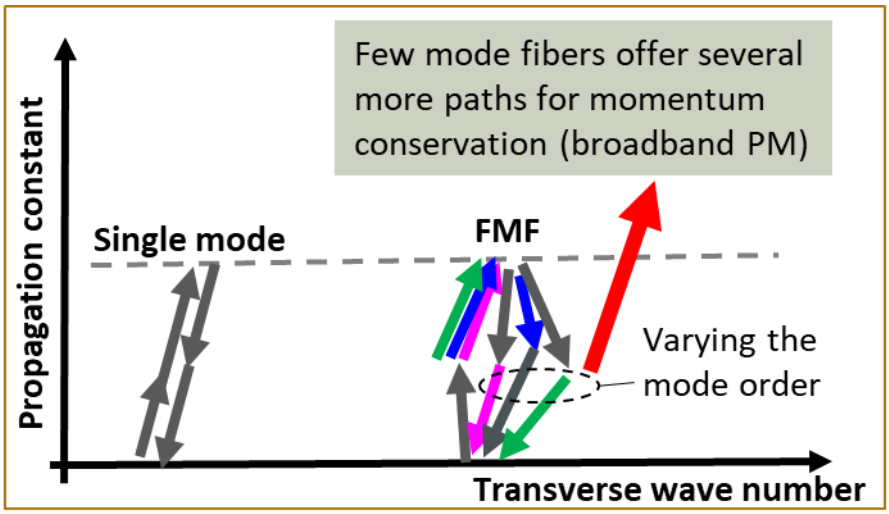

Figure 3. Comparison of FWM in SMF and FMF [31].

As it can be seen in Figure 3, there is a narrow path to satisfy PM condition in the SMF, while FMFs offer several more paths for momentum conservation, so that PM condition could be

satisfied in a more broadband regime compared to SMF. This is because in FMFs spatial modes have, in general, different propagation constants, as shown in Figure 3, which makes it possible to have $\Delta\beta=0$ by simply propagating different waves in different fiber modes [32]. Here we consider a general case IM-FWM in a fiber that supports 2 spatial modes LP_{01} and LP_{11}, as shown in Figure 4.

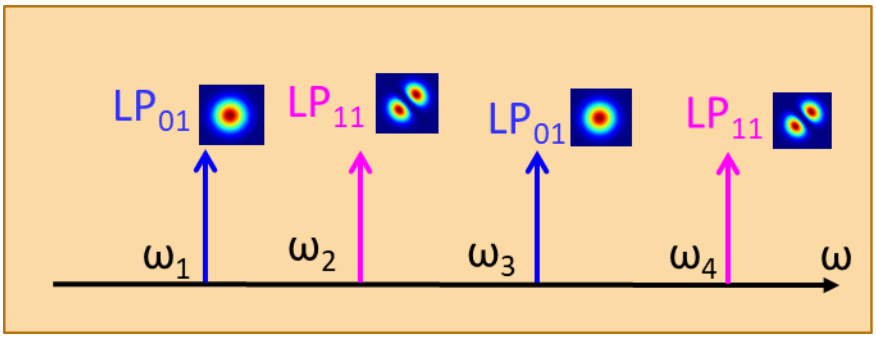

Figure 4. General case of IM-FWM, where signal and pump 2 are in LP_{01} mode, and pump 1 and idler are in LP_{11} mode.

We try to redo the derivation of the PM condition using Taylor's expansion and for simplicity only consider terms up to second order in this section, as it has been done in [28]. With respect to equation (2.3) PM condition is as follows:

$$\Delta\beta = \beta^{(01)}(\omega_1) - \beta^{(11)}(\omega_2) - \beta^{(01)}(\omega_3) + \beta^{(11)}(\omega_4) \approx 0 \qquad (2.5)$$

PM condition will be:

$$\beta^{(11)}(\omega_4) = \beta^{(11)}(\omega_2) + \beta^{(01)}(\omega_3) - \beta^{(01)}(\omega_1) \qquad (2.6)$$

In equation (2.4) $\Delta\omega = \omega - \omega_0$, $\beta_n^{(i)}(\omega) = d^n\beta^{(i)}(\omega)/d\omega^n$, and $\beta_n^{(i)} = \beta_n^{(i)}(\omega)|_{\omega=\omega_0}$ with $n \in \{0,1,2,\ldots\}$.

After expansion, each term in equation (2.6) is:

$$
\begin{aligned}
\beta^{(01)}(\omega_1) &= \beta_0^{(01)}(\omega_0) + \beta_1^{(01)}(\omega_0)\left(\omega_1 - \omega_0\right) + \frac{1}{2}\beta_2^{(01)}(\omega_0)\left(\omega_1 - \omega_0\right)^2 \\
\beta^{(11)}(\omega_2) &= \beta_0^{(11)}(\omega_0) + \beta_1^{(11)}(\omega_0)\left(\omega_2 - \omega_0\right) + \frac{1}{2}\beta_2^{(11)}(\omega_0)\left(\omega_2 - \omega_0\right)^2 \\
\beta^{(01)}(\omega_3) &= \beta_0^{(01)}(\omega_0) + \beta_1^{(01)}(\omega_0)\left(\omega_3 - \omega_0\right) + \frac{1}{2}\beta_2^{(01)}(\omega_0)\left(\omega_3 - \omega_0\right)^2 \\
\beta^{(11)}(\omega_4) &= \beta_0^{(11)}(\omega_0) + \beta_1^{(11)}(\omega_0)\left(\omega_4 - \omega_0\right) + \frac{1}{2}\beta_2^{(11)}(\omega_0)\left(\omega_4 - \omega_0\right)^2
\end{aligned}
\tag{2.7}
$$

By substituting them in equation (2.6) we would have:

$$
\begin{aligned}
&\beta_0^{(11)}(\omega_0) + \beta_1^{(11)}(\omega_0)\left(\omega_4 - \omega_0\right) + \frac{1}{2}\beta_2^{(11)}(\omega_0)\left(\omega_4 - \omega_0\right)^2 \\
&= \beta_0^{(11)}(\omega_0) + \beta_1^{(11)}(\omega_0)\left(\omega_2 - \omega_0\right) + \frac{1}{2}\beta_2^{(11)}(\omega_0)\left(\omega_2 - \omega_0\right)^2 \\
&+\beta_0^{(01)}(\omega_0) + \beta_1^{(01)}(\omega_0)\left(\omega_3 - \omega_0\right) + \frac{1}{2}\beta_2^{(01)}(\omega_0)\left(\omega_3 - \omega_0\right)^2 \\
&-\left[\beta_0^{(01)}(\omega_0) + \beta_1^{(01)}(\omega_0)\left(\omega_1 - \omega_0\right) + \frac{1}{2}\beta_2^{(01)}(\omega_0)\left(\omega_1 - \omega_0\right)^2\right]
\end{aligned}
\tag{2.8}
$$

$\beta_0^{(01)}(\omega_0)$, $\beta_1^{(01)}(\omega_0)*\left(\omega_0\right)$, $\beta_0^{(11)}(\omega_0)$, and $\beta_1^{(11)}(\omega_0)*\left(\omega_0\right)$ terms cancel out for two sides, and the result is:

$$
\begin{aligned}
&\beta_1^{(11)}(\omega_0)\omega_4 + \frac{1}{2}\beta_2^{(11)}(\omega_0)\left(\omega_4 - \omega_0\right)^2 \\
&= \beta_1^{(11)}(\omega_0)\omega_2 + \frac{1}{2}\beta_2^{(11)}(\omega_0)\left(\omega_2 - \omega_0\right)^2 \\
&+\beta_1^{(01)}(\omega_0)\omega_3 + \frac{1}{2}\beta_2^{(01)}(\omega_0)\left(\omega_3 - \omega_0\right)^2 \\
&-\left[\beta_1^{(01)}(\omega_0)\omega_1 + \frac{1}{2}\beta_2^{(01)}(\omega_0)\left(\omega_1 - \omega_0\right)^2\right]
\end{aligned}
\tag{2.9}
$$

After finding common terms for each side, it becomes:

$$
\begin{aligned}
&\beta_1^{(11)}(\omega_0)\left(\omega_4 - \omega_2\right) + \frac{1}{2}\beta_2^{(11)}(\omega_0)\left[\left(\omega_4 - \omega_0\right)^2 - \left(\omega_2 - \omega_0\right)^2\right] \\
&= \\
&\beta_1^{(01)}(\omega_0)\left(\omega_3 - \omega_1\right) + \frac{1}{2}\beta_2^{(01)}(\omega_0)\left[\left(\omega_3 - \omega_0\right)^2 - \left(\omega_1 - \omega_0\right)^2\right]
\end{aligned}
\tag{2.10}
$$

By expanding the brackets, it will be:

$$\begin{aligned}&\beta_1^{(11)}(\omega_0)\left(\omega_4-\omega_2\right)+\frac{1}{2}\beta_2^{(11)}(\omega_0)\left[\left(\omega_4^2-2\omega_4\omega_0+\omega_0^2\right)-\left(\omega_2^2-2\omega_2\omega_0+\omega_0^2\right)\right]\\&=\\&\beta_1^{(01)}(\omega_0)\left(\omega_3-\omega_1\right)+\frac{1}{2}\beta_2^{(01)}(\omega_0)\left[\left(\omega_3^2-2\omega_3\omega_0+\omega_0^2\right)-\left(\omega_1^2-2\omega_1\omega_0+\omega_0^2\right)\right]\end{aligned}\tag{2.11}$$

By organizing the brackets again, we have:

$$\begin{aligned}&\beta_1^{(11)}(\omega_0)\left(\omega_4-\omega_2\right)+\frac{1}{2}\beta_2^{(11)}(\omega_0)\left[-\left(\omega_2^2-\omega_4^2\right)+2\omega_0\left(\omega_2-\omega_4\right)\right]\\&=\\&\beta_1^{(01)}(\omega_0)\left(\omega_3-\omega_1\right)+\frac{1}{2}\beta_2^{(01)}(\omega_0)\left[-\left(\omega_1^2-\omega_3^2\right)+2\omega_0\left(\omega_1-\omega_3\right)\right],\end{aligned}\tag{2.12}$$

which is:

$$\begin{aligned}&\beta_1^{(11)}(\omega_0)\left(\omega_4-\omega_2\right)+\frac{1}{2}\beta_2^{(11)}(\omega_0)\left[-\left(\omega_2-\omega_4\right)\left(\omega_2+\omega_4\right)+2\omega_0\left(\omega_2-\omega_4\right)\right]\\&=\\&\beta_1^{(01)}(\omega_0)\left(\omega_3-\omega_1\right)+\frac{1}{2}\beta_2^{(01)}(\omega_0)\left[-\left(\omega_1-\omega_3\right)\left(\omega_1+\omega_3\right)+2\omega_0\left(\omega_1-\omega_3\right)\right].\end{aligned}\tag{2.13}$$

Again, by finding common factors in the brackets, it will become:

$$\begin{aligned}&\beta_1^{(11)}(\omega_0)\left(\omega_4-\omega_2\right)+\frac{1}{2}\beta_2^{(11)}(\omega_0)\left(\omega_2-\omega_4\right)\left(2\omega_0-\omega_2-\omega_4\right)\\&=\\&\beta_1^{(01)}(\omega_0)\left(\omega_3-\omega_1\right)+\frac{1}{2}\beta_2^{(01)}(\omega_0)\left(\omega_1-\omega_3\right)\left(2\omega_0-\omega_1-\omega_3\right)\end{aligned}\tag{2.14}$$

by taking common factor of (ω_1-ω_4) and (ω_2-ω_3), it is:

$$\begin{aligned}&\left(\omega_2-\omega_4\right)\left[\frac{1}{2}\beta_2^{(11)}(\omega_0)\left(2\omega_0-\omega_2-\omega_4\right)-\beta_1^{(11)}(\omega_0)\right]\\&=\left(\omega_1-\omega_3\right)\left[\frac{1}{2}\beta_2^{(01)}(\omega_0)\left(2\omega_0-\omega_1-\omega_3\right)-\beta_1^{(01)}(\omega_0)\right].\end{aligned}\tag{2.15}$$

From energy conservation equation (2.1), we know that (ω_2–ω_4) = (ω_1–ω_3), so they cancel out each other, and equation (2.5) will be:

$$\beta_1^{(11)}(\omega_0)+\beta_2^{(11)}(\omega_0)\left(\frac{\omega_2+\omega_4-2\omega_0}{2}\right)$$
$$=$$
$$\beta_1^{(01)}(\omega_0)+\beta_2^{(01)}(\omega_0)\left(\frac{\omega_1+\omega_3-2\omega_0}{2}\right),$$

or

$$\beta_1^{(11)}(\omega_0)+\beta_2^{(11)}(\omega_0)\left(\frac{\omega_2-\omega_0+\omega_4-\omega_0}{2}\right)$$
$$=$$
$$\beta_1^{(01)}(\omega_0)+\beta_2^{(01)}(\omega_0)\left(\frac{\omega_1-\omega_0+\omega_3-\omega_0}{2}\right).$$

(2.16)

This leads to the final equation for the PM condition of IM-FWM which is:

$$\beta_1^{(11)}(\omega_0)+\beta_2^{(11)}(\omega_0)\left(\frac{\Delta\omega_2+\Delta\omega_4}{2}\right)=\beta_1^{(01)}(\omega_0)+\beta_2^{(01)}(\omega_0)\left(\frac{\Delta\omega_1+\Delta\omega_3}{2}\right), \quad (2.17)$$

where $\beta_1(\omega)=\beta_1(\omega_0)+\beta_2(\omega_0)\times(\omega-\omega_0)$ is the inverse group velocity at frequency ω for each spatial mode. Equation (2.17) expresses that the phase matching of IM-FWM is achieved when the group velocities evaluated at the average frequencies of the two waves present in each spatial mode are equal. Another important point of it is that PM of the IM-FWM in FMFs is independent of β_0.

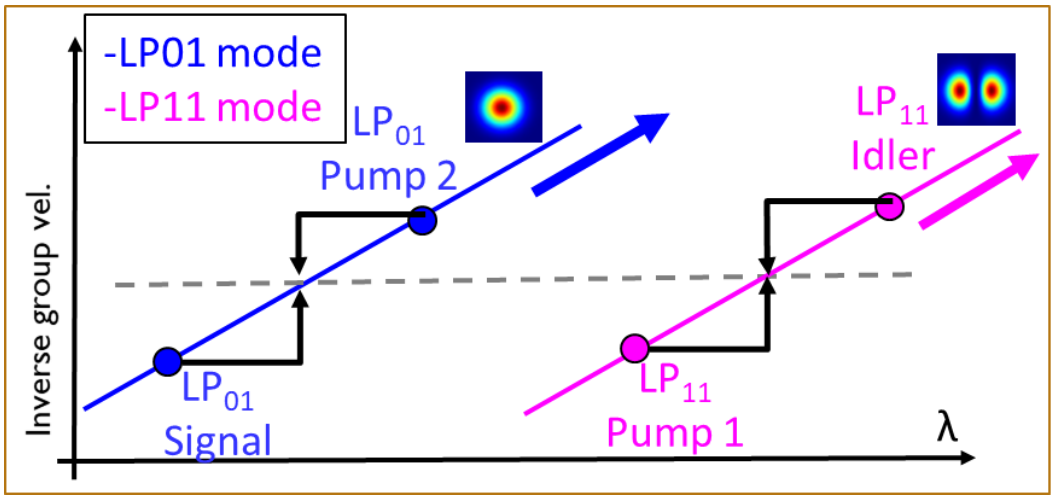

Figure 5. Inverse group velocity of LP_{01} and LP_{11} mode [6].

Figure 5 visualizes the PM condition for a case where signal, pump 1, pump 2, and idler correspond to ω_1, ω_2, ω_3, and ω_4, respectively. It shows that when the inverse group velocities of both modes, evaluated at the average wavelengths of the waves in the same mode, are identical, IM-FWM can take place. It also shows that broadband operation can be achieved if the inverse group velocity curves can be maintained parallel, i.e., if they have similar dispersions.

2.2 Dispersion measurement

As we mentioned in the previous section, the phase matching of IM-FWM is achieved when the group velocities evaluated at the average frequencies of the two waves present in each spatial mode are equal. For that we need to have a fiber that supports more than one spatial mode. Also, we need to measure its dispersion for different modes at different wavelengths.

We have a 1-km long graded-index elliptical core fiber supporting LP_{01} and LP_{11} modes, which has been generously provided to us by Dr. Francesca Parmigiani (formerly with the University of Southhampton; currently with Microsoft Research). The fiber core ellipticity (10%)

breaks degeneracy of LP_{11a} and LP_{11b} modes, so our fiber supports 3 non-degenerate spatial modes LP_{01}, $LP_{11a,}$ and LP_{11b} shown in Figure 6. We will refer to this fiber as three-mode fiber (TMF).

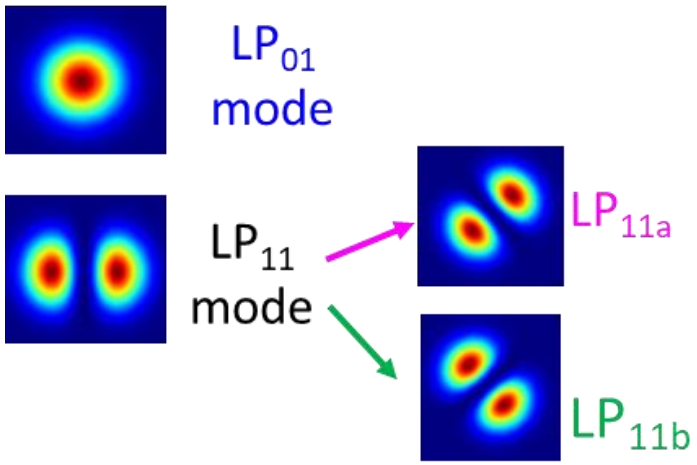

Figure 6. Three non-degenerate spatial modes LP_{01}, $LP_{11a,}$ and LP_{11b} supported by our FMF.

We measured the dispersion of each mode as it is shown in Figure 7. The Agilent chromatic dispersion measurement machine that we have in the lab only transmits and accepts fundamental mode. To measure dispersion for higher-order modes, we coupled the light into free space using a fiber collimator and coverted it to higher-order mode using a phase plate. The higher-order mode is coupled to the fiber using a lens. After propagating in the fiber, it is outcoupled and converted back to the fundamental mode using another phase plate. It is coupled to a single-mode fiber via a fiber collimator and then goes to the dispersion measurement machine. Since this machine only gives dispersion (i.e., group-delay slope) of each spatial mode, we measure group delay of the modes with respect to each other in another procedure.

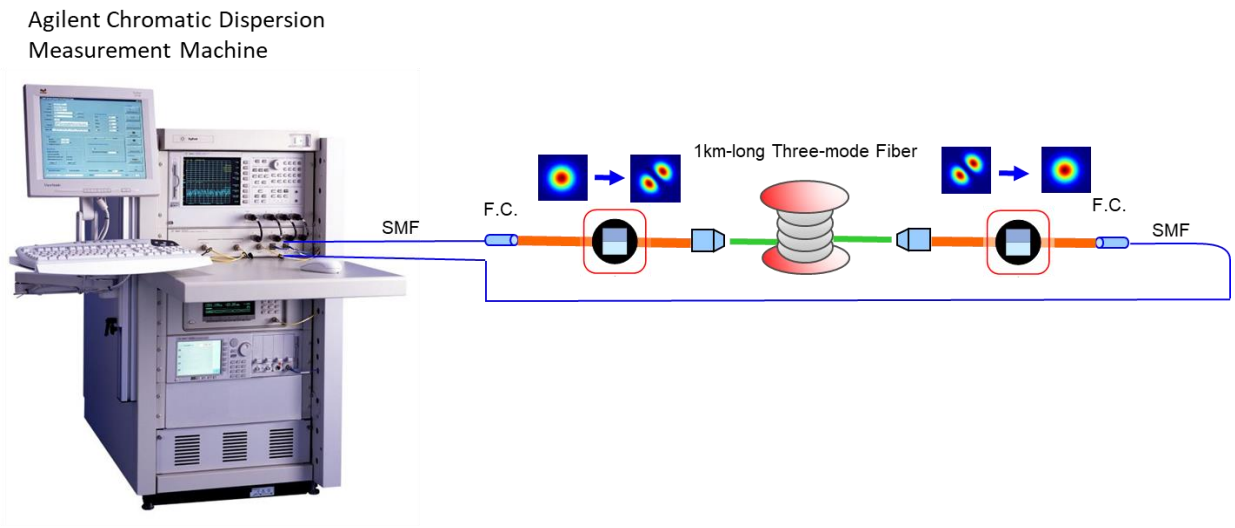

Figure 7. Dispersion measurement setup of different spatial modes.

Figure 8 shows group delay measurement of the spatial modes. A continuous-tunable laser is intensity-modulated at frequency of 1 GHz with an RZ signal with 10% duty cycle and propagates into the free space using a fiber collimator. It is coupled to the FMF using a lens. The beam is slightly angled, so it excites all 3 spatial modes in the FMF. A part of each mode is coupled into SMF and goes to a fast photodetector. The output of the photodetector is read by a sampling oscilloscope. As a result of different group velocity, each mode arrives at the detector at a different time.

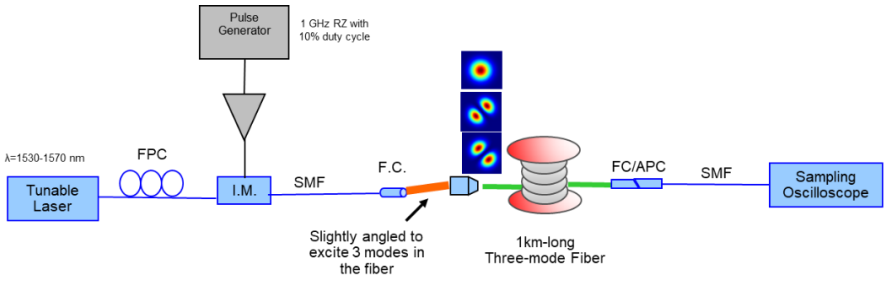

Figure 8. Experimental setup of group delay measurement of 3 spatial modes in the FMF.

Figure 9a shows measured relative inverse group velocities (RIGV) $1/v_g$ of LP_{01}, LP_{11a}, and LP_{11b} modes of our TMF. The LP_{11a}, and LP_{11b} curves are approximately parallel to the LP_{01} curve

and horizontally shifted from it by ~24 nm ($\Delta\nu_1$ = 3 THz) and ~41 nm ($\Delta\nu_2$ = 5.1 THz). Figure 9b shows the group delays between LP_{01}, LP_{11a}, and LP_{11b} modes, which are represented as the vertical separation between relative inverse group velocities in Figure 9b.

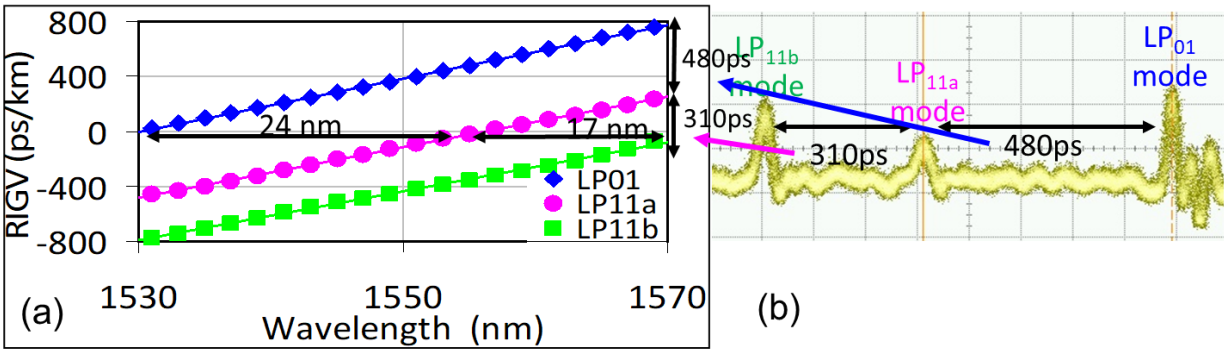

Figure 9. (a) Measured relative inverse group velocity (RIGV) data for the modes of our TMF (b) group delays between LP_{01}, LP_{11a}, and LP_{11b} modes.

2.3 Theory of $\chi^{(3)}$-based mode-selective frequency conversion

Our scheme of $\chi^{(3)}$-based mode-selective frequency conversion employs a combination of two IM-FWM processes illustrated in Fig. 10a. We use an elliptical-core FMF [6] that supports three non-degenerate modes (LP_{01}, LP_{11a}, and LP_{11b}), to be referred to as three-mode fiber (TMF) below. In IM-FWM process 1, pumps 1 and 2 upconvert LP_{11a} signal to LP_{01} output mode. In process 2, pumps 3 and 4 upconvert LP_{01} signal to the same LP_{01} output mode. With all 4 pumps present, a selected superposition of signal LP_{01} and LP_{11a} modes is upconverted, whereas the orthogonal mode superposition is left unperturbed. Selection of the mode superposition is done by choosing relative powers of the 2 pairs of pump waves (i.e., relative weights of processes 1 and 2) and pump phase difference $\Delta\varphi = (\varphi_{p1} - \varphi_{p2}) - (\varphi_{p3} - \varphi_{p4})$. Energy conservation and phase-matching

conditions for each process need to be satisfied. Energy conservation laws for wavelength-converted signal (denoted by subscript "WC") in processes 1 and 2 are as follows:

$$\text{(Process 1)} \qquad \nu_{WC} = \nu_S + \nu_{P1} - \nu_{P2}\,, \qquad (2.18)$$

$$\text{(Process 2)} \qquad \nu_{WC} = \nu_S + \nu_{P3} - \nu_{P4} \qquad (2.19)$$

where ν is the optical frequency for each wave, and subscripts "*S*" and "*Pi*" denote the signal and i^{th} pump waves, respectively.

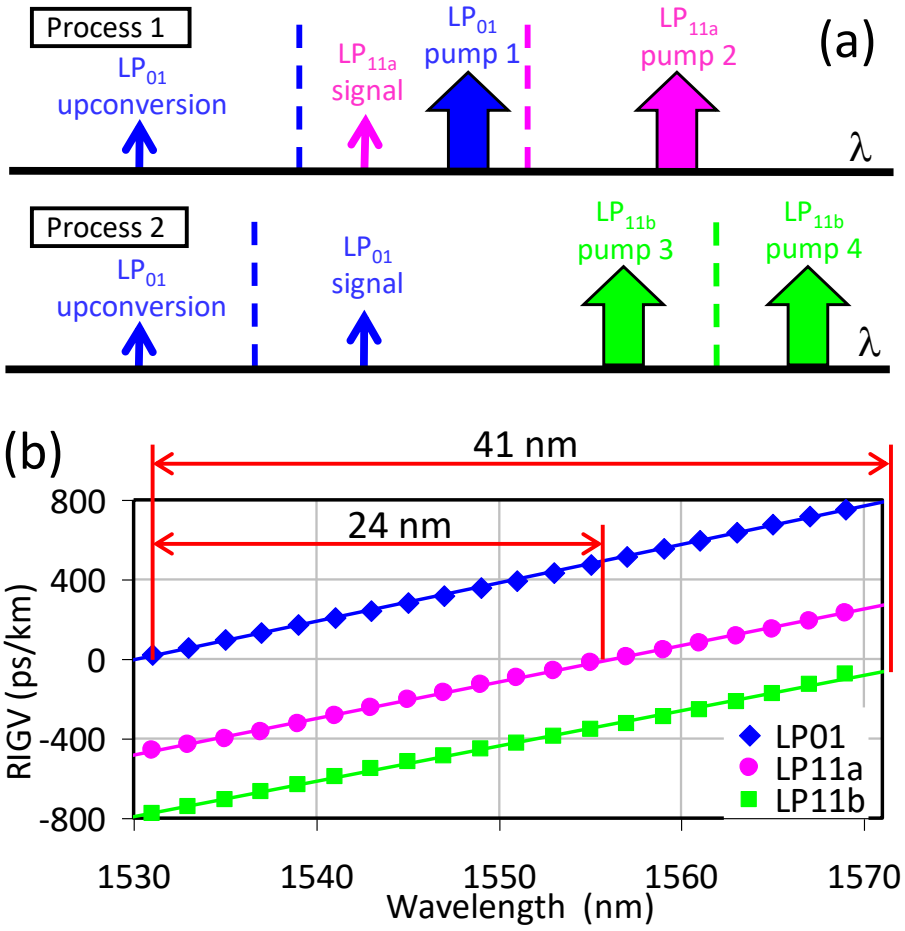

Figure 10. (a) Two parametric processes, whose combination enables mode-selective frequency upconversion in the TMF. (b) Measured relative inverse group velocity (RIGV) data for the mode of our TMF.

IM-FWM selection rules [33] require preservation of the total number of photons in each spatial mode for each process. The phase matching conditions are given by:

$$\text{(Process 1)}\quad \beta^{(01)}(\omega_{WC}) = \beta^{(11a)}(\omega_S) + \beta^{(01)}(\omega_{P1}) - \beta^{(11a)}(\omega_{P2}) \quad (2.20)$$

$$\text{(Process 2)}\quad \beta^{(01)}(\omega_{WC}) = \beta^{(01)}(\omega_S) + \beta^{(11b)}(\omega_{P3}) - \beta^{(11b)}(\omega_{P4}) \quad (2.21)$$

where β is the propagation constant of each wave, and $\omega = 2\pi\nu$. After Taylor's expansion of $\beta^{(i)}(\omega)$, the phase-matching condition can be reduced to

$$\text{(Process 1)}\qquad \beta_1^{(01)}\left(\frac{\omega_{WC}+\omega_{P1}}{2}\right) = \beta_1^{(11a)}\left(\frac{\omega_S+\omega_{P2}}{2}\right) \qquad (2.22)$$

$$\text{(Process 2)}\qquad \beta_1^{(01)}\left(\frac{\omega_{WC}+\omega_S}{2}\right) = \beta_1^{(11b)}\left(\frac{\omega_{P3}+\omega_{P4}}{2}\right) \qquad (2.23)$$

where β_1 denotes the inverse group velocity $1/v_g$.

Phase-matching conditions (2.22), (2.23) mean that, for each process, the group velocities at the average frequencies of the two waves present in each spatial mode must be equal [33]. These average frequencies, converted to wavelengths, are shown by the dashed lines in Fig. 10a. Figure 10b shows measured relative inverse group velocities (RIGV) $1/v_g$ of LP_{01}, LP_{11a}, and LP_{11b} modes of our TMF. The LP_{11a} and LP_{11b} curves are approximately parallel to the LP_{01} curve and are horizontally shifted from it by ~24 nm ($\Delta\nu_1$ = 3 THz) and ~41 nm ($\Delta\nu_2$ = 5.1 THz), respectively. Thus, phase matching is satisfied when the dashed lines in Figure 10b are separated by 24 nm and 41 nm for processes 1 and 2, respectively, so that we have:

$$\text{(Process 1)}\qquad \frac{\nu_{WC}+\nu_{P1}}{2} - \frac{\nu_S+\nu_{P2}}{2} = \Delta\nu_1 \qquad (2.24)$$

(Process 2) $$\frac{\nu_{WC}+\nu_S}{2}-\frac{\nu_{P3}+\nu_{P4}}{2}=\Delta\nu_2 \qquad (2.25)$$

To satisfy the energy conservation and phase-matching conditions for both processes simultaneously, we have solved the system of Eqs. (2.18), (2.19), (2.24), and (2.25) which has resulted in the following 4 constraints on the frequencies of the 6 involved waves: $\nu_{P1} - \nu_{P2} = \nu_{P3} - \nu_{P4} = \nu_{WC} - \nu_S = \Delta\nu_1$ and $\nu_S = \nu_{P3} + \Delta\nu_2 - \Delta\nu_1$, where ν_S (or ν_{P3}) and ν_{P1} (or ν_{P2}) can be chosen arbitrarily.

2.4 Theory of $\chi^{(3)}$-based spatial-mode entanglement

Our spatial-mode entanglement scheme employs a combination of two IM-FWM processes of Figure 11. We use an elliptical-core FMF [6] that supports three non-degenerate modes (LP_{01}, LP_{11a}, and LP_{11b}), to be referred to as three-mode fiber (TMF) below. In IM-FWM process 1, with the help of pumps 1 and 2 a signal photon is created in mode LP_{01} at frequency ν_S, while idler photon is created in mode LP_{11a} at frequency ν_I. In process 2, their roles interchange: in the presence of pumps 3 and 4, signal photon at frequency ν_S is created in mode LP_{11a}, whereas the idler photon at frequency ν_I is created in mode LP_{01}. With all 4 pumps present, both processes occur simultaneously. Their probabilities can be equalized by adjusting relative powers of the two pump pairs, which leads to generation of the maximally-entangled state $|LP_{01}\rangle_S|LP_{11a}\rangle_I + e^{i\varphi}|LP_{11a}\rangle_S|LP_{01}\rangle_I$, where phase φ can be changed by varying the pump phase difference $\Delta\varphi = (\varphi_{P1} + \varphi_{P2}) - (\varphi_{P3} + \varphi_{P4})$. Subscript "*Pi*" denotes i^{th} pump wave. This scheme represents a spatial-mode generalization of the Kwiat's original polarization-entanglement scheme [34] that used a sequence of two thin down-conversion crystals oriented with 90-degree angle between their optical axes, with pump at 45 degrees with respect to either axis. Just as there is no way to tell which crystal has produced a given photon pair, there is also no way to tell which of the two IM-FWM processes

has produced a given photon pair, which results in generation of the superposition of the states yielded by the two processes. Energy conservation and phase matching conditions need to be satisfied for each process. Energy conservation laws for processes 1 and 2 are as follows:

(Process 1) $$\nu_I = \nu_{P1} + \nu_{P2} - \nu_S \quad (2.26)$$

(Process 2) $$\nu_I = \nu_{P3} + \nu_{P4} - \nu_S \quad (2.27)$$

where ν is the optical frequency for each wave. IM-FWM selection rules [33] require preservation of the total number of photons in each spatial mode for each process. The phase matching conditions are given by:

(Process 1) $$\beta^{(11a)}(\omega_I) = \beta^{(01)}(\omega_{P1}) + \beta^{(11a)}(\omega_{P2}) - \beta^{(01)}(\omega_S) \quad (2.28)$$

(Process 2) $$\beta^{(01)}(\omega_I) = \beta^{(01)}(\omega_{P3}) + \beta^{(11a)}(\omega_{P4}) - \beta^{(11a)}(\omega_S) \quad (2.29)$$

After Taylor expansion of $\beta^{(i)}(\omega)$, the phase-matching condition can be reduced to

(Process 1) $$\beta_1^{(01)}\left(\frac{\omega_S + \omega_{P1}}{2}\right) = \beta_1^{(11a)}\left(\frac{\omega_I + \omega_{P2}}{2}\right) \quad (2.30)$$

(Process 2) $$\beta_1^{(01)}\left(\frac{\omega_I + \omega_{P3}}{2}\right) = \beta_1^{(11a)}\left(\frac{\omega_S + \omega_{P4}}{2}\right) \quad (2.31)$$

where β_1 denotes the inverse group velocity $1/v_g$.

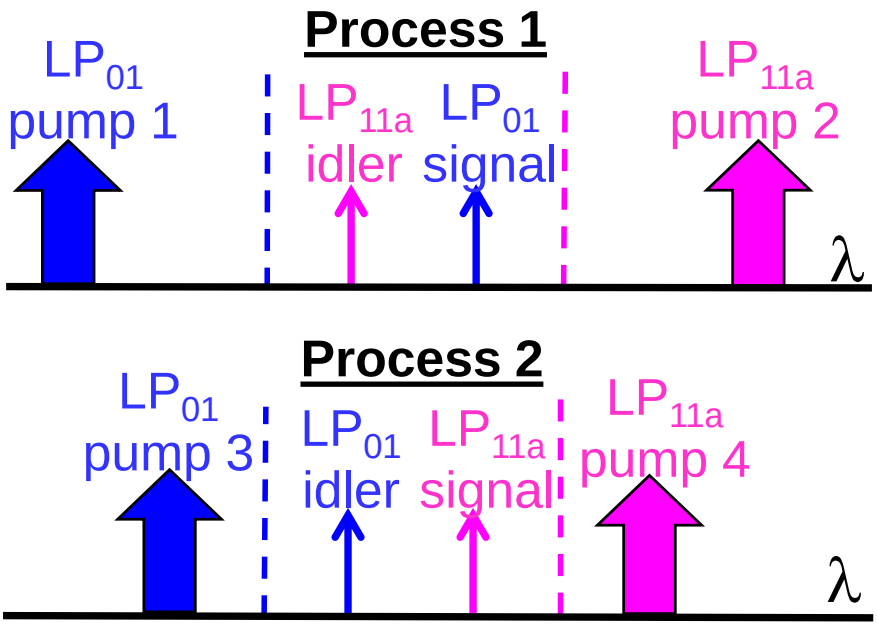

Figure 11. Two parametric processes, whose combination enables generation of spatial-mode-entangled signal-idler photon pairs in the TMF.

Phase-matching conditions (2.30), (2.31) mean that, for each process, the group velocities at the average frequencies of the two waves present in each spatial mode must be equal [33]. These average frequencies, converted to wavelengths, are shown by the dashed lines in Figure 11. Figure 10b shows measured relative inverse group velocities (RIGV) $1/v_g$ of LP_{01}, LP_{11a}, and LP_{11b} modes of our TMF. The LP_{11a} and LP_{11b} curves are approximately parallel to the LP_{01} curve and are horizontally shifted from it by ~24 nm ($\Delta\nu_1$ = 3 THz) and ~41 nm ($\Delta\nu_2$ = 5.1 THz), respectively. Thus, phase matching is satisfied when the dashed lines in Fig. 1 are separated by 24 nm, so that we have:

(Process 1) $$\frac{\nu_S + \nu_{P1}}{2} - \frac{\nu_I + \nu_{P2}}{2} = \Delta\nu_1 \qquad (2.32)$$

(Process 2) $$\frac{\nu_I + \nu_{P3}}{2} - \frac{\nu_S + \nu_{P4}}{2} = \Delta\nu_1 \qquad (2.33)$$

To satisfy energy conservation and phase-matching conditions for both processes simultaneously, we have solved the system of Eqs. (2.26), (2.27), (2.32), and (2.33), which has resulted in the following 4 constraints on the frequencies of the 6 involved waves: $\nu_{p1(p3)} = \nu_{i(s)} + \Delta\nu_1$ and $\nu_{p2(p4)} = \nu_{s(i)} - \Delta\nu_1$. Here, any two frequencies that are not separated by $\Delta\nu_1$ can be arbitrarily chosen.

Based on these scenarios, the $\chi^{(3)}$-based mode-selective frequency conversion and spatial-mode entanglement have been implemented in several stages experimentally. The detailed experiment, discussion and result will be explained in next chapter.

Chapter 3: Experimental Results

In this chapter, we present principles of operation, experimental setups, and results of 3 projects as follows: 1) Mode-selective frequency conversion in a few-mode fiber, 2) Generation of spatially-entangled photon pairs in a few-mode fiber, and 3) OAM-selective frequency conversion and OAM-entangled photon pair generation in a few-mode fiber.

3.1 Mode-selective frequency conversion in a few-mode fiber

In this section, we present a scheme for spatial-mode-selective frequency conversion in a few-mode fiber and experimentally demonstrate upconversion of arbitrary superpositions of LP_{01} and LP_{11a} signal modes from C-band to the fundamental mode in S-band with all conversion efficiencies within 1 dB range of one another.

3.1.1 Principle of operation

As explained in previous chapter, our scheme of $\chi^{(3)}$-based mode-selective frequency conversion employs a combination of two IM-FWM processes illustrated in Figure 12a. We use an elliptical-core FMF [6] that supports three non-degenerate modes: LP_{01}, LP_{11a}, and LP_{11b}, to be referred to as three-mode fiber (TMF) below. In IM-FWM process 1, pumps 1 and 2 upconvert LP_{11a} signal to LP_{01} output mode. In process 2, pumps 3 and 4 upconvert LP_{01} signal to the same LP_{01} output mode. With all pumps 1, 2, 3, and 4 present, a selected superposition of signal LP_{01} and LP_{11a} modes is upconverted, whereas the orthogonal mode superposition is left unperturbed. For each process, the phase-matching condition [33] requires equal group velocities at the average frequencies of the two waves present in each spatial mode. These average frequencies, converted to wavelengths, are shown by dashed lines in Figure 12a. Figure 12b shows measured relative inverse group velocities (RIGV) $1/v_g$ of LP_{01}, LP_{11a}, and LP_{11b} modes of our TMF. The LP_{11a}, and

LP_{11b} curves are approximately parallel to the LP_{01} curve and horizontally shifted from it by ~24 nm ($\Delta\nu_1$ = 3 THz) and ~41 nm ($\Delta\nu_2$ = 5.1 THz), respectively. Thus, the phase matching is satisfied when the dashed lines in Fig. 1a are separated by 24 nm and 41 nm for processes 1 and 2, respectively. Energy conservation and phase matching put the following 4 constraints on the frequencies of the 6 involved waves: $\nu_{p1} - \nu_{p2} = \nu_{p3} - \nu_{p4} = \nu_{WC} - \nu_s = \Delta\nu_1$ and $\nu_s = \nu_{p3} + \Delta\nu_2 - \Delta\nu_1$, where ν_s (or ν_{p3}) and ν_{p1} (or ν_{p2}) can be chosen arbitrarily, and subscript "WC" stands for wavelength-converted output.

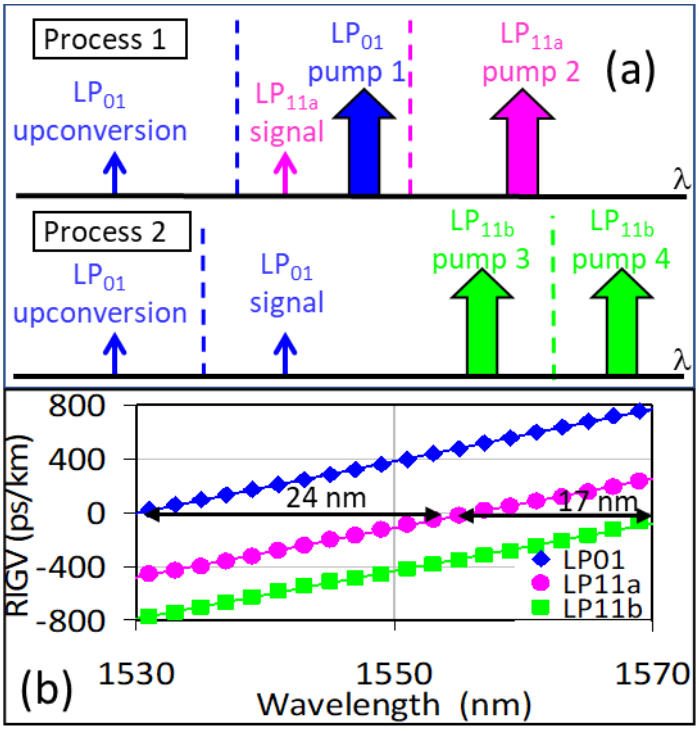

Figure 12. (a)Two parametric processes, whose combination enables mode-selective frequency upconversion in the TMF. (b) Measured relative inverse group velocity (RIGV) data for the modes of our TMF.

3.1.2 Demonstration of IM-FWM Processes 1 and 2 individually

In this section we implement two IM-FWM Processes 1 and 2 individually. In our experiment, we convert C-band signal at 1540 nm to S-band (1516.4 nm), using wavelengths 1552, 1576.4, 1556.9, and 1581.9 nm for pumps 1, 2, 3, and 4, respectively.

3.1.2.1 Experimental setup

Our experimental setup is shown in Figure 13. The signal and pumps are carved into 10-ns-long flat-top pulses with a 10-MHz repetition rate by 3 intensity modulators and are amplified by telecom-grade C- and L-band erbium-doped fiber amplifiers (EDFAs). In process 1, signal and pump 2 are combined with a WDM coupler, converted to LP_{11a} mode via a phase plate PP1, combined with pump 1 in LP_{01} mode by a beam splitter, and coupled into the 1-km-long TMF by an objective. TMF output is collimated by a second objective. Part of the output is observed on an infrared camera, and the remaining part is coupled into a single-mode fiber (SMF) connected to the optical spectrum analyzer (OSA), which in this case measures the LP_{01} "output port" of the TMF. By inserting phase plate PP3 prior to SMF coupling, we can also measure LP_{11a} "output port" of the TMF. In process 2, pumps 3 and 4 are WDM multiplexed, converted to LP_{11b} mode via a phase plate PP2, combined with signal in LP_{01} mode by a beam splitter, and coupled into the TMF similarly to process 1. To maximize IM-FWM, we co-polarize all three input waves in each process via polarization controllers (PCs) and polarization beam splitter PBS. Mode selectivity of each process is investigated by injecting the input signal into a wrong (undesirable) mode (LP_{01} in process 1, LP_{11a} in process 2).

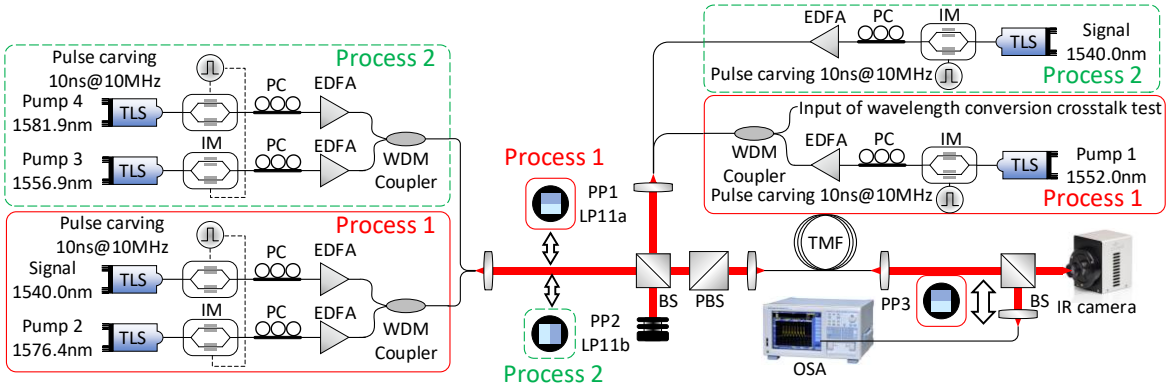

Figure 13. Mode-selective frequency conversion in a three-mode fiber experimental setup.

3.1.2.2 Mode selectivity and conversion efficiencies with/without proper spatial mode of signal

Figure 14 shows the spectra at the LP_{01} output port of the TMF for processes 1. The conversion efficiency (CE) for the desired signal mode is –40.3 dB in process 1, primarily limited by relatively low pump powers coupled into the TMF. Figure 15 shows the spectra at the LP_{01} output port of the TMF for processes 1 when signal is in the undesirable mode. The CE for the undesirable signal mode is 15.5 dB lower than the corresponding desired-mode CEs in this process. This number represents low amount of crosstalk from the undesirable input signal mode, which indicates good mode selectivity of our scheme. Average powers inside the TMF are 0 dBm for the signal in all cases and 16, 13 dBm for pumps 1 and 2.

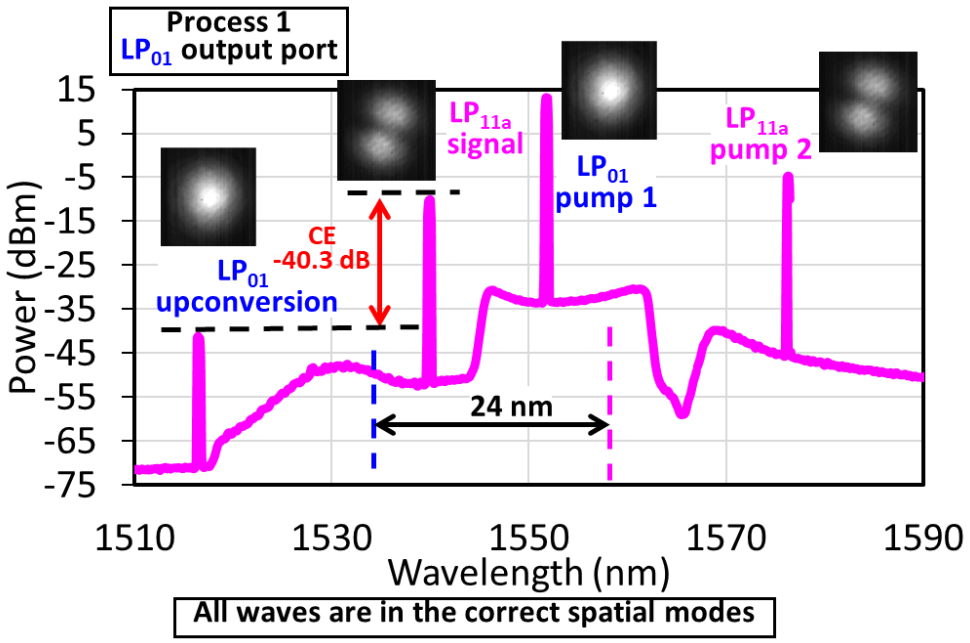

Figure 14. Experimental results measured at the LP_{01} "output port" of the TMF for processes 1.

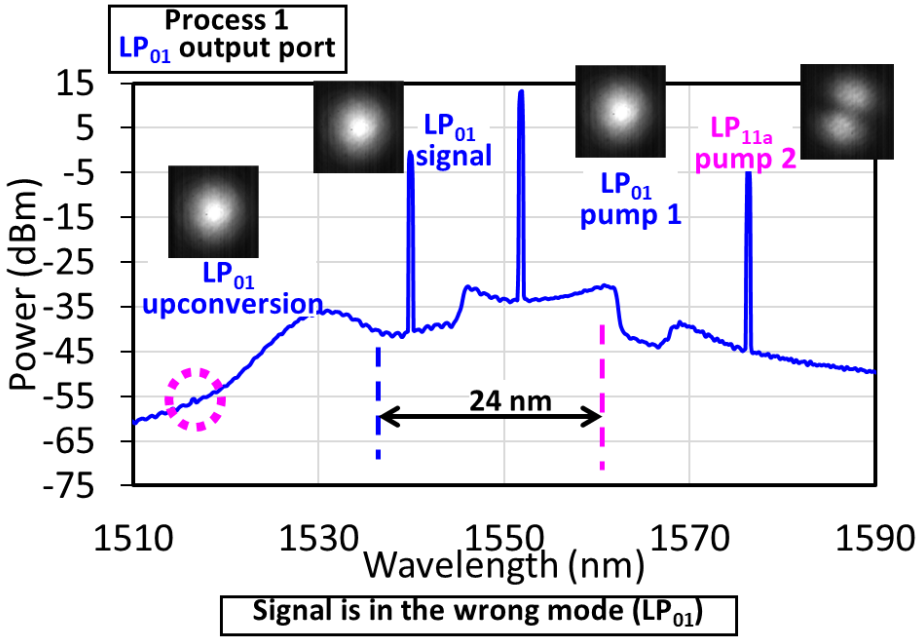

Figure 15. Experimental results measured at the LP_{01} "output port" of the TMF for processes 1 when signal is in the wrong mode LP_{01}.

Figure 16 shows the spectra at the LP_{01} output port of the TMF for processes 2. The conversion efficiency (CE) for the desired signal mode is –37.8 dB in process 2, primarily limited by relatively

low pump powers coupled into the TMF. Figure 17 shows the spectra at the LP_{01} output port of the TMF for processes 2 when signal is in the undesirable mode. The CE for the undesirable signal mode is 20 dB lower than the corresponding desired-mode CEs in this process. This number represents low amount of crosstalk from the undesirable input signal mode, which indicates good mode selectivity of our scheme. Average powers inside the TMF are 0 dBm for the signal in all cases and 15.5, 13.8 dBm for pumps 3 and 4.

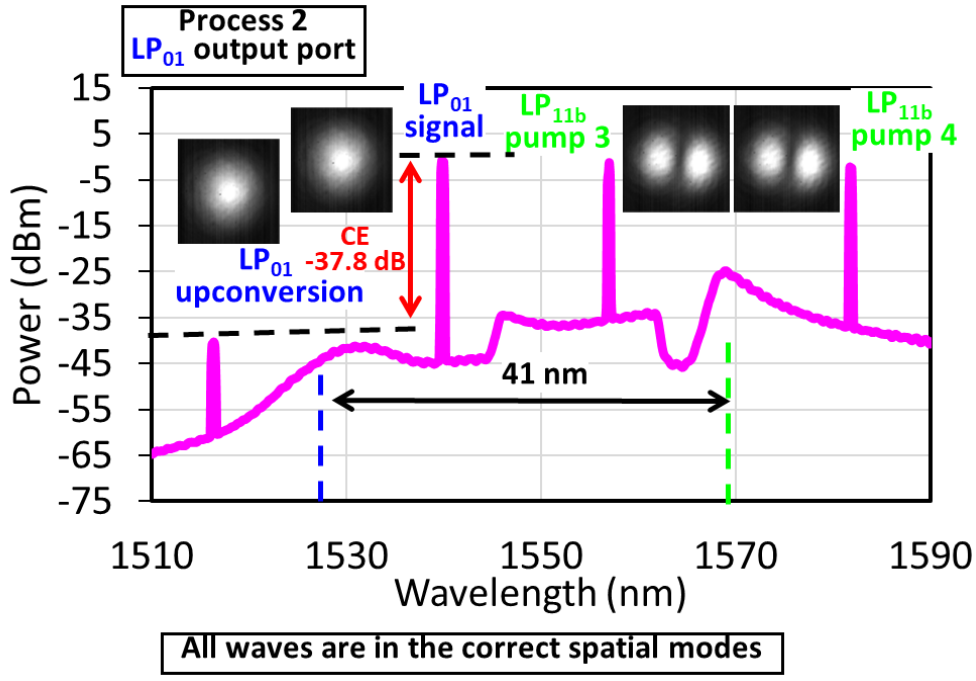

Figure 16. Experimental results measured at the LP_{01} "output port" of the TMF for processes 2.

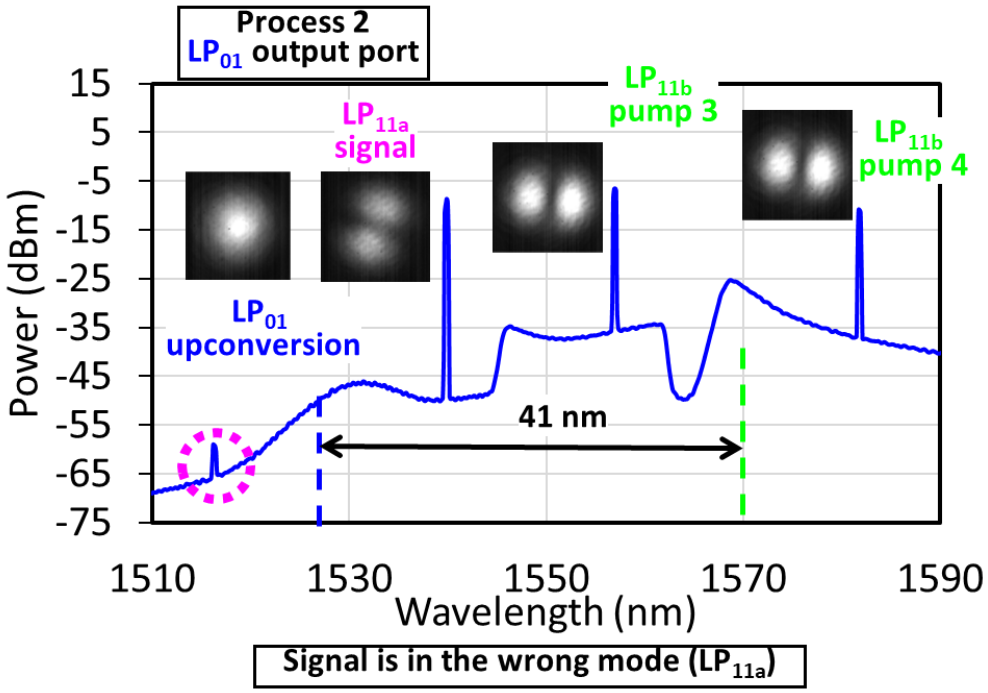

Figure 17. Experimental results measured at the LP_{01} "output port" of the TMF for processes 2 when signal is in the wrong mode LP_{11a}.

3.1.2.3 Spatial mode demultiplexing and mode purity

Spatial mode demultiplexing of the WC signal for each spatial mode is done by reading the power from LP_{01} and LP_{11a} ports. Purple spectrum in Figure 18 is read from LP_{01} output port, and blue spectrum is read from LP_{11a} output port of the TMF in process 1. By comparing these two spectra, we have measured the mode purity of the wavelength-converted signal to be better than 14.8 dB, which shows quality of our spatial mode demultiplexing. For process 2, as it is shown in Figure 19, the mode purity of the wavelength-converted signal is better than 13.9 dB. These numbers show that the WC signal in desired spatial mode can be generated and spatially distinguished from other spatial modes with mode purity of better than 14 dB, which is a quite acceptable for quantum communication applications as well as in optical communication.

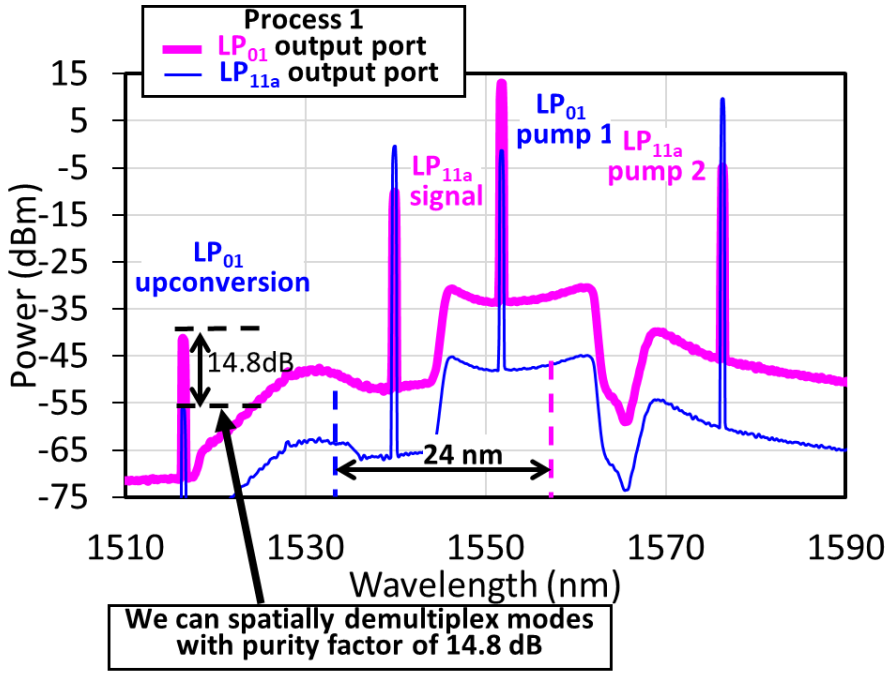

Figure 18. Spatial mode demultiplexing of the WC signal by reading from LP_{01} and LP_{11a} ports in process 1.

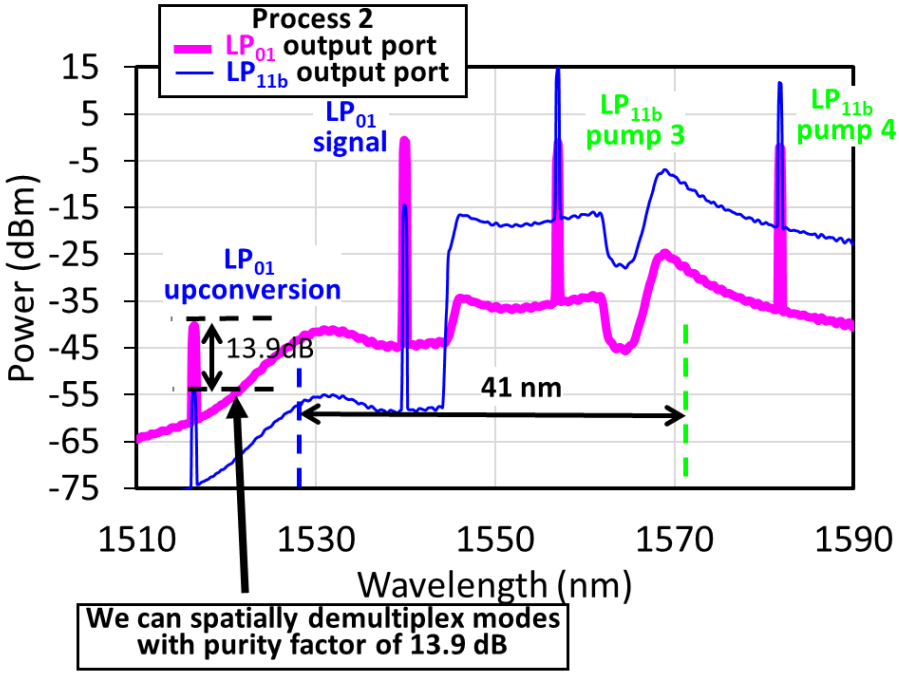

Figure 19. Spatial mode demultiplexing of the WC signal by reading from LP_{01} and LP_{11a} ports in process 2.

3.1.2.4 Results

To summarize this experiment, we have experimentally demonstrated selective upconversion of either LP_{01} or LP_{11a} signal wave from C-band (1540 nm) to a single LP_{01} wave in S-band (1516.4 nm) with two pairs of pumps in different spatial mode configurations. These results have shown good crosstalk performance (mode selectivity) for each of the two IM-FWM processes individually. Next step would be to implement both of these two processes simultaneously and demonstrate their combined ability to handle any mode superposition in the two-mode signal space. In the next section, we show how two IM-FWM processes would be implemented simultaneously for mode-selective frequency conversion.

3.1.3 Mode-selective frequency conversion with Processes 1 and 2 running simultaneously

As mentioned above, in this section we implement both two processes simultaneously. All the theory for this is also the same as explained above. In this experiment, we convert C-band signal at 1542.9 nm to S-band (1519.5 nm), using wavelengths 1554.4, 1578.7, 1560.4, and 1585.1 nm for pumps 1, 2, 3, and 4, respectively.

3.1.3.1 Experimental setup

Figure 20 shows our experimental setup. All pumps and the signal are carved into 10-ns-long flat-top pulses with 10-MHz repetition rate by 3 intensity modulators. The pumps are then amplified by telecom-grade C- and L-band erbium-doped fiber amplifiers (EDFAs). Pump 2 is converted to LP_{11a} mode by a phase plate PP1, combined with pump 1 in free space by beam splitter BS1, and combined with pumps 3 and 4, which have been converted to LP_{11b} mode by a phase plate PP2, by free-space beam splitter BS2. All the pumps are combined with the signal by a dichroic beam splitter and coupled into the 1-km-long TMF by an objective. The TMF output is split between an infrared camera and a single-mode fiber (SMF) connected to the optical spectrum

analyzer (OSA), which in this case measures the LP_{01} "output port" of the TMF. By inserting phase plate PP4 prior to SMF coupling, we can also measure LP_{11a} "output port" of the TMF. We can gradually vary the signal spatial mode from LP_{01} to LP_{11a} by vertically moving the phase plate PP3 (when it is centered on the beam, it generates LP_{11a} mode; when it is far off the center, it leaves the mode in LP_{01}; in the intermediate positions it generates various two-mode superpositions). To maximize IM-FWM, we co-polarize all three input waves in each process.

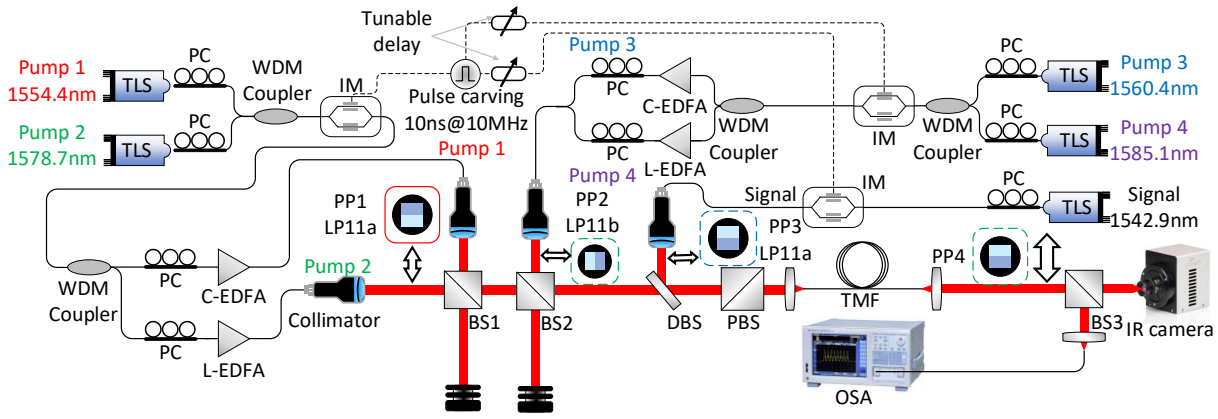

Figure 20. Two parametric processes, whose combination enables mode-selective frequency upconversion in the TMF.

3.1.3.2 Mode selectivity and conversion efficiencies with/without proper spatial mode of signal

Mode selectivity of each individual process is quantified by comparing conversion efficiency (CE) for the "desired" signal mode (LP_{11a} in process 1, LP_{01} in process 2) to the CE for the "undesirable" signal mode (LP_{01} in process 1, LP_{11a} in process 2). Inverse of the mode selectivity represents the crosstalk from the undesirable signal mode. Figure 21a shows the spectra illustrating the mode selectivity in process 1, amounting to 20.5 dB. Figure 21b shows 19.8 dB mode selectivity in process 2. In each process, the conversion efficiencies are measured by comparing the power level of the wavelength-converted signal to the power of the original signal. They are found to be –44.3 and –42.7 dB for processes 1 and 2, respectively.

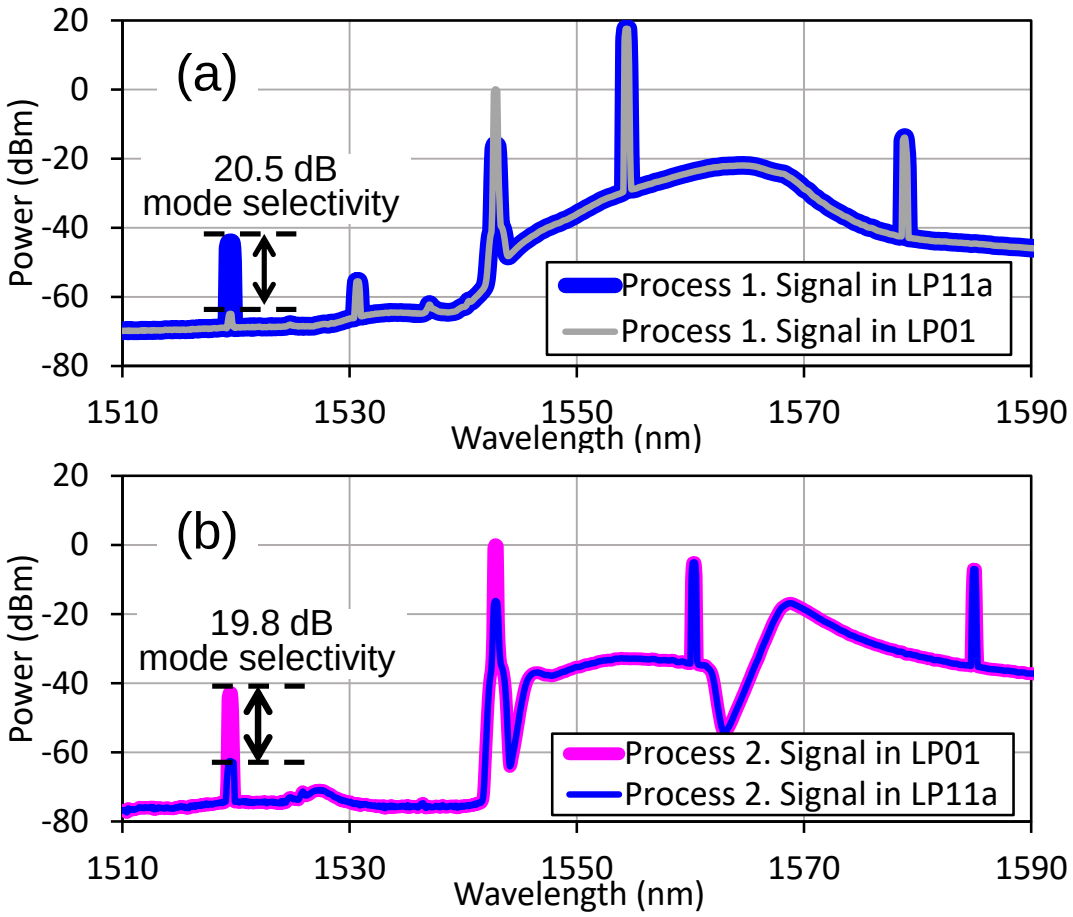

Figure 21. (a) Optical spectra for process 1 with input signal in either LP_{11a} (thick blue) or LP_{01} (thin gray) mode. (b) Optical spectra for process 2 with input signal in either LP_{11a} (thin blue) or LP_{01} (thick purple) mode. For both graphs, the spectra are measured at the LP_{01} "output port" of the TMF.

Figure 22 shows the mode-selective frequency conversion spectra with all 4 pumps present (i.e., with both IM-FWM processes 1 and 2 taking place simultaneously), where the spatial mode profile of each wave is also shown. Signal spatial mode can be either LP_{01} or LP_{11a} mode, or any superposition of them (the spectra shown in Figure 22 are obtained with signal in LP_{01} mode). Pump powers have been tuned to nearly equalize the CEs for both processes. Blue spectrum in Figure 22 is read from LP_{01} output port, and purple spectrum is read from LP_{11a} output port of the TMF. By comparing these two spectra, we have measured the mode purity of the wavelength-converted signal to be better than 14.5 dB. Average powers inside the TMF are 0 dBm for the

signal and 17.5, 2.0, 9.5, and 7.5 dBm for pumps 1, 2, 3, and 4, respectively. At these powers, the CEs for processes 1 and 2 are nearly equal (within 0.8 dB of each other).

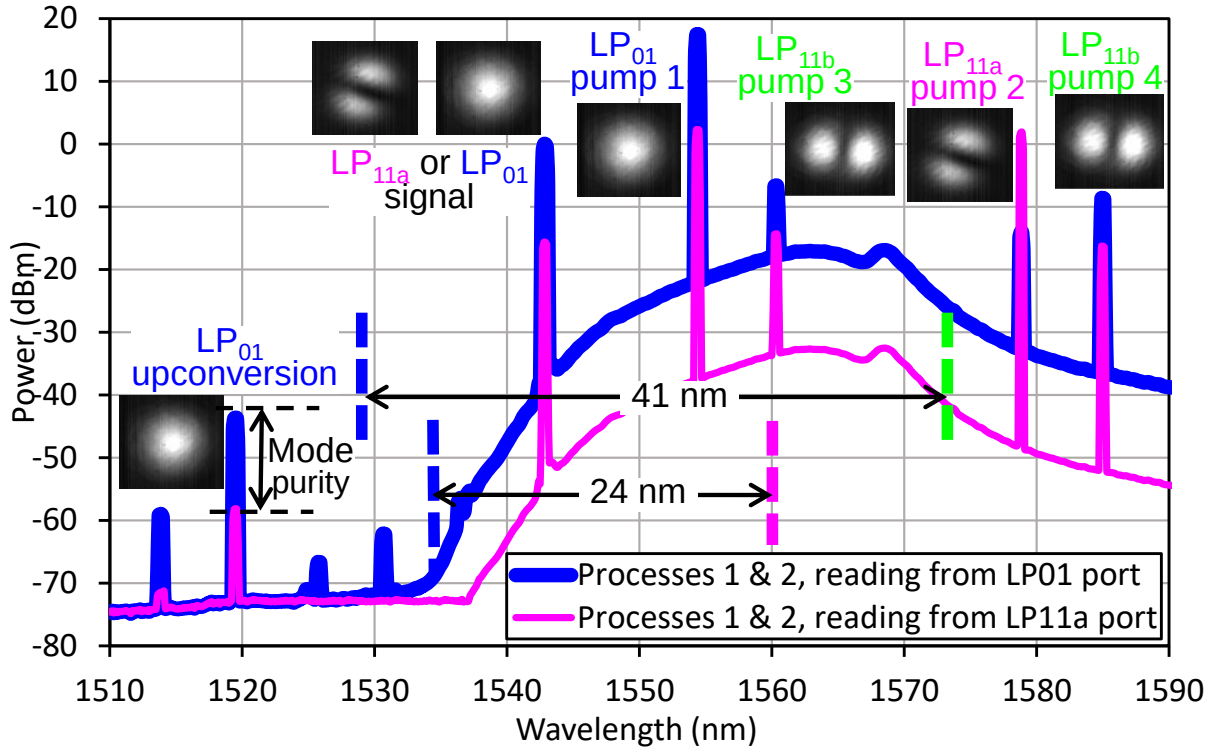

Figure 22. Spectra of processes 1 and 2 taking place simultaneously and observed through LP_{01} (thick blue) and LP_{11a} (thin purple) output ports. In our experiments, the signal input can be in either LP_{01} or LP_{11a} mode, or any superposition of them. The spectra shown correspond to the input signal in LP_{01} mode.

If we had stable phase $\Delta\varphi = (\varphi_{p1} - \varphi_{p2}) - (\varphi_{p3} - \varphi_{p4})$, we would have been able to select for upconversion a superposition of LP_{01} and LP_{11a} modes with a specific relative phase. However, such stabilization (based on optical comb) has not been implemented in our setup yet, and our $\Delta\varphi$ fluctuates randomly on 0.1–1 μs scale. This means that we can observe mode-independent signal upconversion to LP_{01}, as both LP_{01} and LP_{11a} components of any signal superposition are independently upconverted to LP_{01} and added incoherently. This is illustrated in Figure 23, which shows nearly the same CEs (within 1 dB range from one another) measured for various signal superpositions with weight of LP_{11a} component ranging from 0 to 100%.

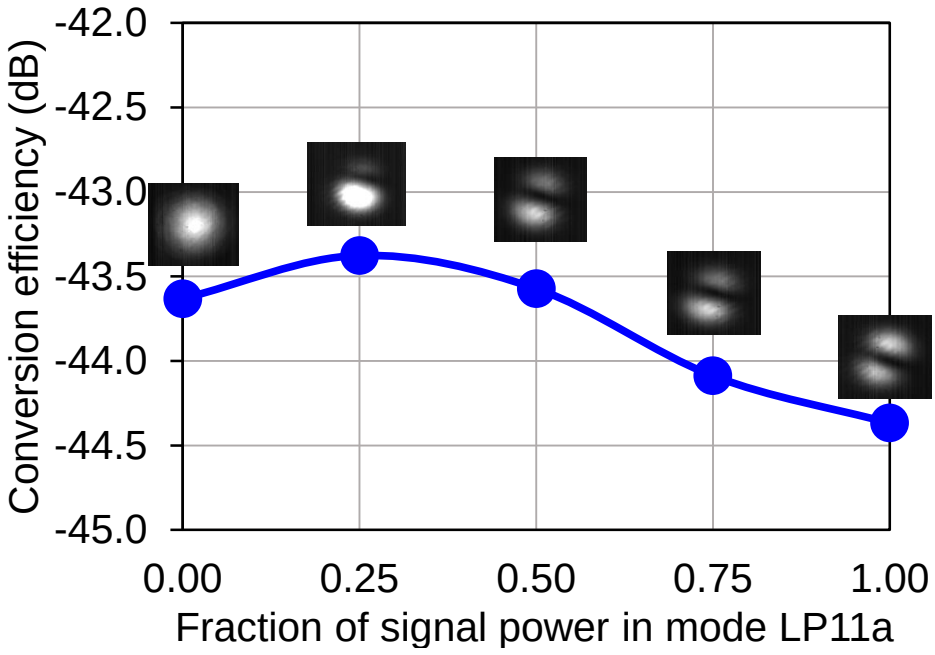

Figure 23. Conversion efficiencies for various signal mode superpositions.

3.1.4 Summary of mode-selective frequency conversion in a three-mode fiber

At first, we have implemented two inter-modal four-wave-mixing processes individually, which are necessary for achieving spatial-mode-selective frequency conversion in (LP_{01}, LP_{11a}) mode space. Then, we have simultaneously implemented these two inter-modal four-wave-mixing processes necessary for achieving reconfigurable spatial-mode-selective frequency conversion in (LP_{01}, LP_{11a}) mode space. For these two processes, we have demonstrated conversion efficiencies of –44.3 dB and –42.7 dB and mode selectivities (inverse crosstalk) of 20.5 dB and 19.8 dB, respectively. We have also shown that, in the absence of pump phase stabilization, this scheme can produce mode-independent signal frequency conversion for various superpositions of signal's LP_{01} and LP_{11a} modes. To increase the conversion efficiencies in the future, one could employ higher-power EDFAs and, possibly, a customized few-mode fiber with a reduced core size and higher nonlinearity.

3.2 Generation of spatially-entangled photon pairs in a few-mode fiber

In this section, we describe a scheme for generation of spatial-mode-entangled photon pairs in a few-mode fiber and experimentally demonstrate generation of idler beams from classical seed signals representing various superpositions of fiber LP_{01} and LP_{11a} modes. For every signal mode superposition, we observe the indication of idler mode orthogonality to the signal mode.

3.2.1 Principle of operation

As explained in detail in Chapter 2, our spatial-mode entanglement scheme employs a combination of two IM-FWM processes of Figure 24a. We use an elliptical-core FMF [6] that supports three non-degenerate modes: LP_{01}, LP_{11a}, and LP_{11b}, to be referred to as three-mode fiber (TMF) below. In IM-FWM process 1, with the help of pumps 1 and 2 a signal photon is created in mode LP_{01} at frequency ν_s, while idler photon is created in mode LP_{11a} at frequency ν_i. In process 2, their roles interchange: in the presence of pumps 3 and 4, signal photon at frequency ν_s is created in mode LP_{11a}, whereas the idler photon at frequency ν_i is created in mode LP_{01}. With all four pumps present, processes 1 and 2 take place simultaneously. Their probabilities can be equalized by adjusting relative powers of the two pump pairs, which results in generation of the maximally-entangled state $|LP_{01}\rangle_s|LP_{11a}\rangle_i + e^{i\varphi}|LP_{11a}\rangle_s|LP_{01}\rangle_i$, where phase φ can be changed by varying the pump phase difference $\Delta\varphi = (\varphi_{p1} + \varphi_{p2}) - (\varphi_{p3} + \varphi_{p4})$. For each of the two processes in Figure 24a, the phase-matching condition [33] requires equal group velocities at the average frequencies of the two waves present in each spatial mode. These average frequencies, converted to wavelengths, are shown by dashed lines in Figure 24a. Figure 24b shows measured relative inverse group velocities (RIGV) $1/v_g$ of LP_{01}, LP_{11a}, and LP_{11b} modes of our TMF. The LP_{11a} curve is approximately parallel to the LP_{01} curve and horizontally shifted from it by ~25 nm ($\Delta\nu_1$ = 3 THz), i.e., the phase matching is satisfied when the dashed lines in Figure 24a are separated by 25 nm. Energy

conservation and momentum conservation (phase matching) impose 4 constraints on the frequencies of the 6 involved waves: $\nu_{p1(p3)} = \nu_{i(s)} + \Delta\nu_1$ and $\nu_{p2(p4)} = \nu_{s(i)} - \Delta\nu_1$, hence any two frequencies that are not separated by $\Delta\nu_1$ can be arbitrarily chosen.

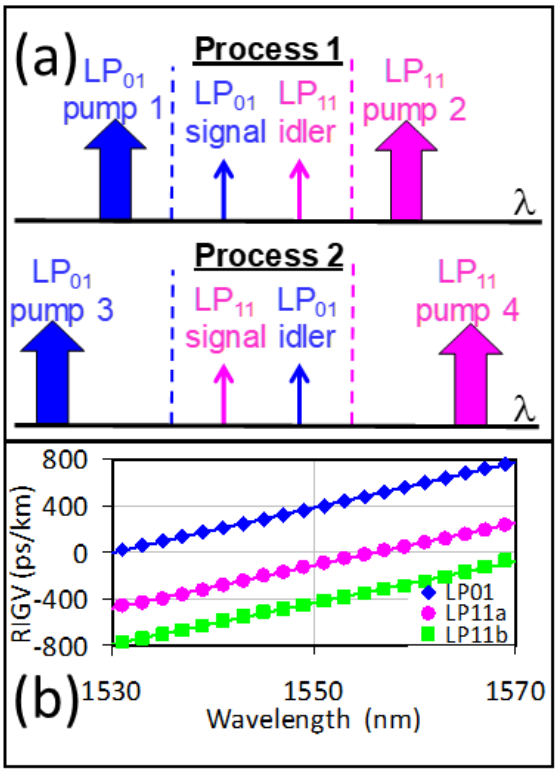

Figure 24. (a) Two parametric processes, whose combination enables generation of spatial-mode-entangled signal-idler photon pairs in the TMF. (b) Measured relative inverse group velocity (RIGV) data for the modes of our TMF.

3.2.2 Demonstration of IM-FWM Processes 1 and 2 individually

In this section we implement two IM-FWM Processes 1 and 2 individually. In our experiment, we choose signal to be at 1562.3 nm and idler to be at 1564.6 nm, which results in pumps 1, 2, 3, and 4 placed at 1540.1, 1587.5, 1538.3, and 1589.3, respectively.

3.2.2.1 Experimental setup

Our experimental setup is shown in Figure 25. The test signal and pumps are carved into 10-ns-long flat-top pulses with a 10-MHz repetition rate by intensity modulators and are amplified by

telecom-grade C- and L-band erbium-doped fiber amplifiers (EDFAs). In process 1, signal and pump 1 are combined with an arrayed waveguide grating (AWG) multiplexer, collimated into a free-space LP_{01} mode, and combined by a beam splitter with pump 2 that has been converted to LP_{11a} mode by a phase plate PP1. The three waves are then coupled into a 1-km-long TMF by an objective. The TMF output is collimated by a second objective. Part of the output is observed on an infrared camera, and the remainder is coupled into a single-mode fiber (SMF) connected to the optical spectrum analyzer (OSA), which in this case measures the LP_{01} "output port" of the TMF. By inserting phase plate PP3 prior to SMF coupling, we can also measure LP_{11a} "output port" of the TMF. In process 2, signal and pump 4 are combined by a WDM coupler, converted to LP_{11a} mode via a phase plate PP2, combined with pump 3 in LP_{01} mode by a beam splitter, and coupled into the TMF similarly to process 1. To maximize IM-FWM, we co-polarize all three input waves in each process via polarization controllers (PCs) and polarization beam splitter (PBS).

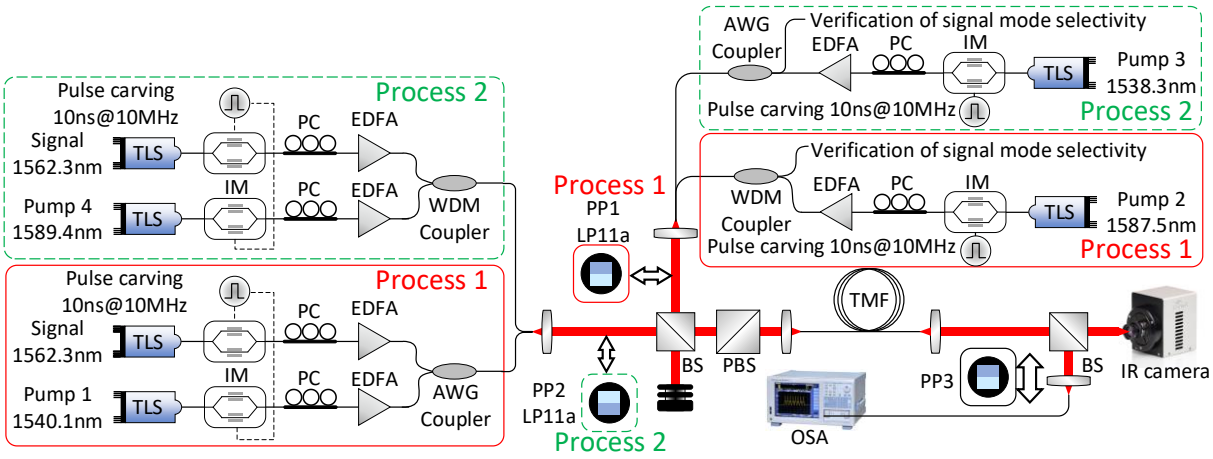

Figure 25. Generation of spatially-entangled photon pairs with classical signal in a three-mode fiber experimental setup.

3.2.2.2 Mode purity and conversion efficiencies with/without proper spatial mode of signal

We characterize idler-mode impurity by comparing idlers in LP_{01} and LP_{11a} output ports of the TMF. The depth of suppression of undesirable parametric interactions, i.e., mode selectivity of

the parametric amplification processes 1 and 2, is quantified by comparing the idler generated by the desired process to that generated by an undesirable process, observed when the input signal is injected into a wrong mode: LP_{11a} for process 1, LP_{01} for process 2. In the former case, this injection is done by combining signal and pump 2 via WDM coupler prior to their conversion to LP_{11a} mode. In the latter case, it is done by combining signal and pump 3 by AWG before the beam splitter.

Figure 26 and Figure 27 show the spectra at the LP_{01} (blue traces) and LP_{11a} (magenta traces) output ports of the TMF for processes 1 and 2, respectively. One can easily see a significant change in the idler power between the two traces, indicating high spatial-mode purity of the idler (23.1 and 17.5 dB for processes 1 and 2, respectively). Average powers inside the TMF are 0 dBm for the signal in all cases and 13, 10.5, 13, and 10.5 dBm for pumps 1, 2, 3, and 4, respectively. Easily-measurable signal-to-idler conversion efficiency is CE = $g - 1 = \langle n \rangle$, where g is the phase-insensitive parametric gain, and $\langle n \rangle$ is the average number of generated parametric photons per mode, also representing the probability of a single pair generation for our case of CE << 1. In Figs. 26 and 27, CEs are equal to –45.2 and –46.2 dB for processes 1 and 2, respectively. The CEs of the undesirable processes, measured by injecting the signal into the wrong mode, are suppressed by 28 and 38 dB, compared to processes 1 and 2, respectively.

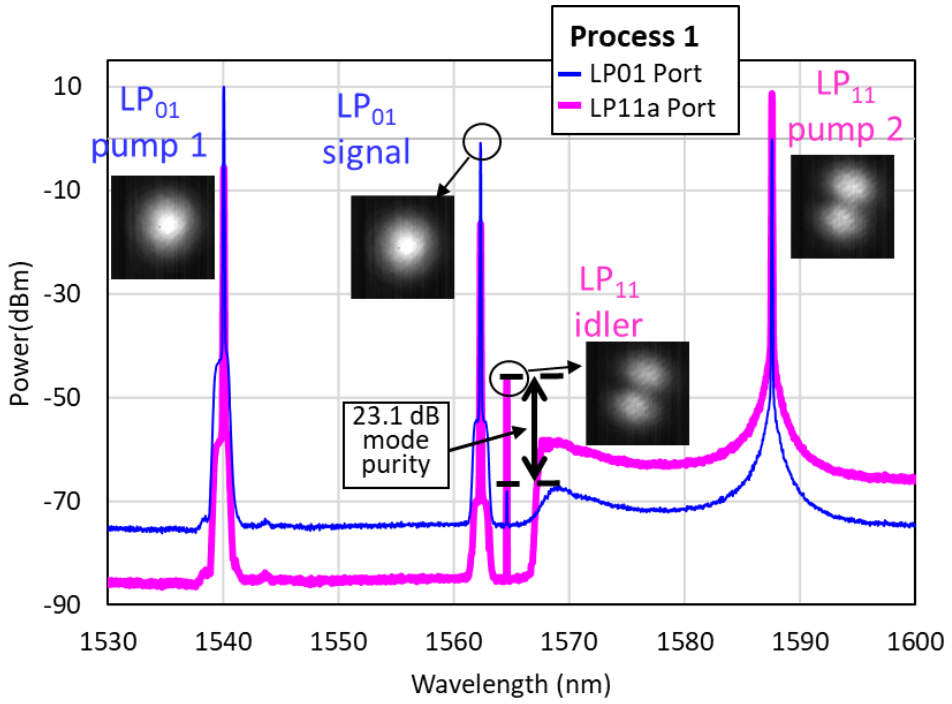

Figure 26. Optical spectra, measured at the LP_{01} (blue traces) and LP_{11a} (purple traces) output ports of the TMF for processes 1 when signal is in LP_{01} mode.

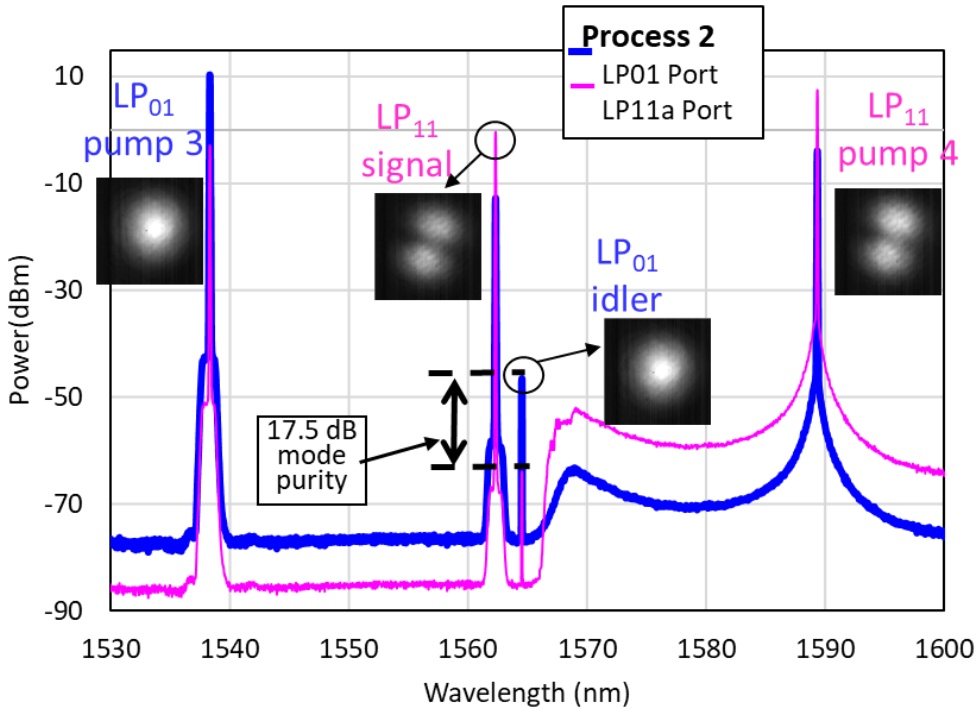

Figure 27. Optical spectra, measured at the LP_{01} (blue traces) and LP_{11a} (purple traces) output ports of the TMF for processes 2 when signal is in LP_{11a} mode.

3.2.2.3 Results

To summarize this part, we experimentally verified the underlying inter-modal parametric processes with two-mode classical signal input and demonstrated high mode purity of the generated idler. We have demonstrated low-gain parametric amplifier in TMF, which couples LP_{01} signal to LP_{11a} idler and LP_{11a} signal to LP_{01} idler with high mode selectivity. In the spontaneous regime, the combination of these two processes would generate spatial-mode-entangled signal-idler photon pairs. The next step is to optimize the pump multiplexing scheme, both to minimize the losses and to use 4 pumps at the same time. We further combine both processes and observe that they couple the input two-mode seed signal to an orthogonal two-mode idler for various signal-mode superpositions.

3.2.3 Generation of spatially-entangled photon pairs with classical signal in a few-mode fiber with two IM-FWM processes simultaneously

As mentioned above, in this section we implement both two processes simultaneously. All the theory for this is also the same as explained above. In previous part using classical seed signals, we experimental measured signal-idler mode selectivity separately for these two processes. In this part, we further combine both processes and observe that they couple the input two-mode seed signal to an orthogonal two-mode idler for various signal-mode superpositions.

3.2.3.1 Experimental setup

Our experimental setup is shown in Figure 28. The pumps 1–4 and signal are carved into 10-ns-long flat-top pulses with a 10-MHz repetition rate by 3 intensity modulators. The pumps are amplified by telecom-grade C- and L-band erbium-doped fiber amplifiers (EDFAs). Amplified pumps 1 and 3 are combined by a 50/50 coupler. Amplified pumps 2 and 4 are combined by a WDM coupler, converted to LP_{11a} mode by a phase plate (PP2), combined with the signal by a

free-space beam splitter (BS1) and with pumps 1 and 3 by a free-space dichroic beam splitter (DBS), and then coupled into the 1-km-long TMF by an objective. TMF output is collimated by a second objective. We split the output between an infrared camera and a single-mode fiber (SMF) connected to the optical spectrum analyzer (OSA), which in this case measures the LP_{01} "output port" of the TMF. By inserting phase plate PP3 prior to the OSA's SMF input, we can also measure LP_{11a} "output port" of the TMF. We can gradually vary the signal spatial mode from LP_{01} to LP_{11a} by vertically moving the phase plate PP1 (when it is centered on the beam, it generates LP_{11a} mode; when it is far off the center, it leaves the mode in LP_{01}; in the intermediate positions it generates various two-mode superpositions). To maximize IM-FWM, we co-polarize all three input waves in each process.

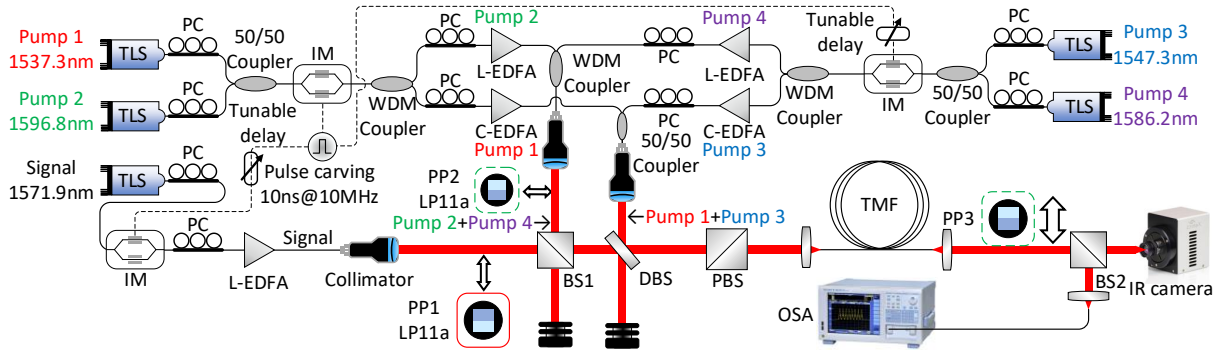

Figure 28. Experimental setup of two parametric processes, whose combination enables generation of spatial-mode-entangled signal-idler photon pairs in the TMF.

3.2.3.2 Mode purity and conversion efficiencies with/without proper spatial mode of signal

Mode selectivity of each process separately is investigated by comparing the idler power generated by the classical seed signal in the "correct" mode (LP_{01} for process 1, LP_{11a} for process 2) to that generated by the signal in the "wrong" mode (LP_{11a} and LP_{01}, respectively). Figure 29a shows the process 1 spectra at the TMF's LP_{11a} output port, exhibiting mode selectivity of 19 dB. Figure 29b shows the process 2 spectra at the TMF's LP_{01} output port, exhibiting mode selectivity better than 9 dB. It is difficult to estimate the selectivity of process 2 more accurately, because the

idler generated by the "wrong" signal is buried deeply below the amplified spontaneous emission (ASE) noise from the EDFAs in the pump paths. We have observed mode selectivities better than 28 dB in [35], where we filtered ASE noise more aggressively.

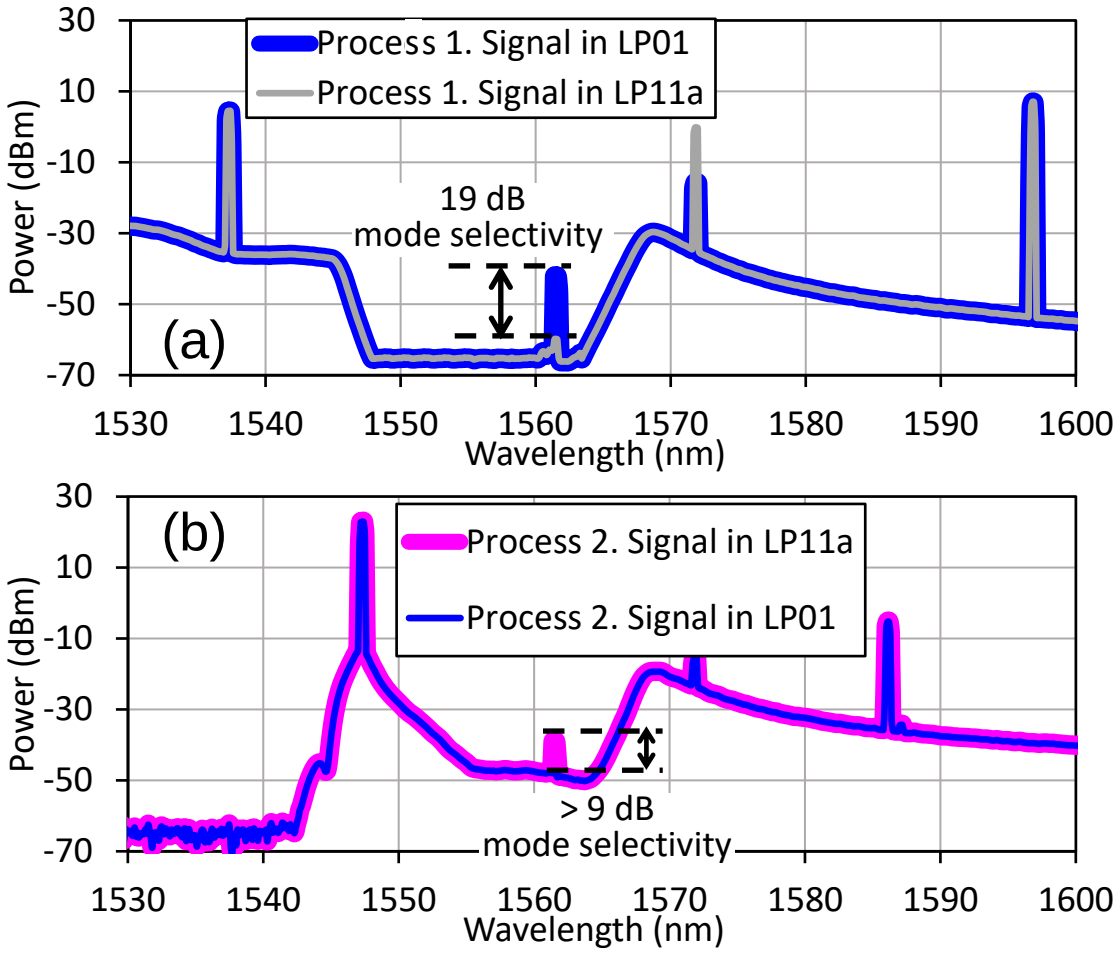

Figure 29. (a) Mode selectivity in process 1 shown by comparing the idler generated at the LP_{11a} output port by the "correct" signal mode LP_{01} to that generated by the "wrong" mode LP_{11a}. (b) Mode selectivity in process 2 shown by comparing the idler generated at the LP_{01} output port by the "correct" signal mode LP_{11a} to that generated by the "wrong" mode LP_{01}.

Figure 30 shows spectra when all 4 pumps are present, i.e., both processes 1 and 2 taking place simultaneously. The results are measured at the LP_{01} output port (thick red) and LP_{11a} output port (thin blue) for signal in LP_{11a} mode. As expected, virtually no idler is present at the LP_{11a} port for such signal input (i.e., idler is deeply buried under the ASE noise). Average powers inside the

TMF are 0 dBm for the signal and 20, 7.5, 20, and 9 dBm for pumps 1, 2, 3, and 4, respectively. In each process, the conversion efficiency is measured by comparing power level of the idler to the power of the original signal. The pump powers are chosen to equalize the signal-to-idler conversion efficiencies (CEs) at –43 dB for processes 1 and 2. CE = $g - 1 = \langle n \rangle$, where g is the parametric gain, and $\langle n \rangle$ is the average number of photons generated per mode in the absence of the seed signal (parametric fluorescence), also equal to the probability of a single-pair generation for CE << 1 (our case).

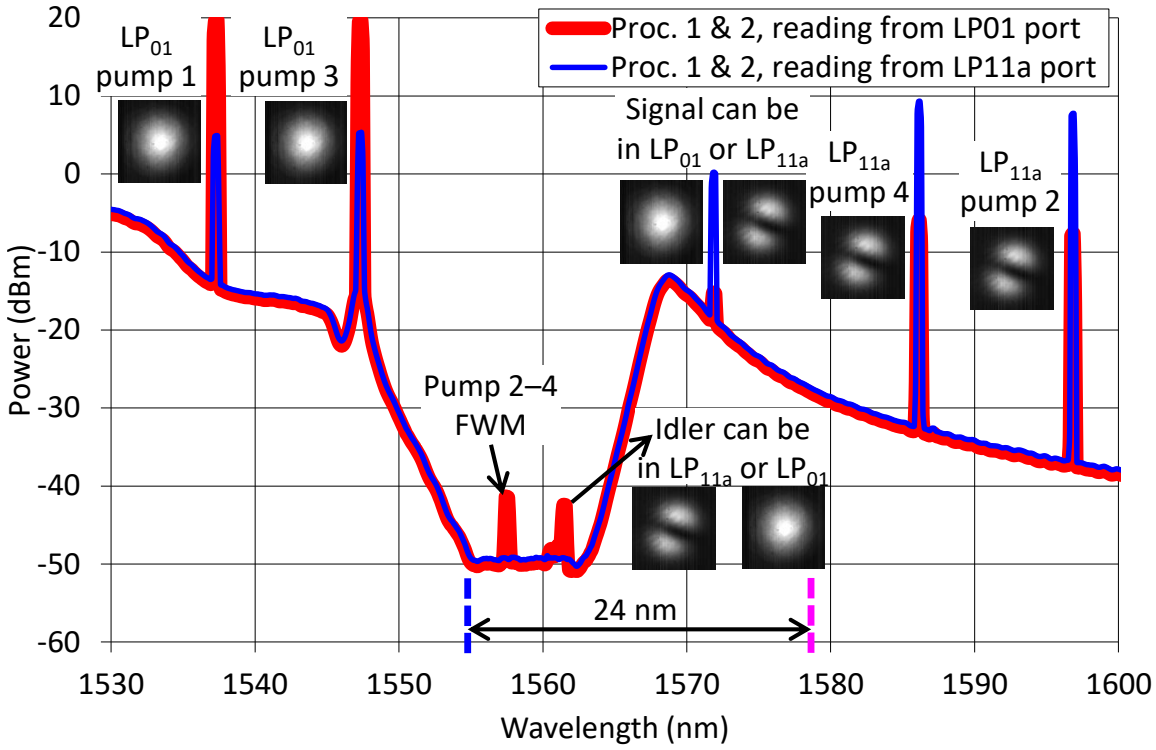

Figure 30. Spectra for processes 1 and 2 occurring simultaneously, with seed signal in LP_{11a} mode, observed through LP_{01} (thick red) and LP_{11a} (thin blue) output ports.

With all 4 pumps present, Figure 31 shows the idler powers at the LP_{01} and LP_{11a} output ports for various two-mode superpositions of the input seed signal, after the ASE noise floor has been subtracted. One can see that, as the weight of LP_{11a} signal mode in the superposition changes from 0 to 100%, the total idler power remains constant (within 1 dB), while the weights of idler

modes LP_{01} and LP_{11a} change from nearly 0 to 100% and from 100% to nearly 0, respectively, as expected for the generated idler mode that is orthogonal to the input signal mode. In the future, we plan to stabilize the phase $\Delta\varphi = (\varphi_{P1} + \varphi_{P2}) - (\varphi_{P3} + \varphi_{P4})$, which would allow us to set the relative phase of the two modes in the idler mode superposition to make it perfectly orthogonal to the signal mode superposition. The mutual coherence of the 4 pumps can be obtained by deriving them from a common optical comb source. Any slow phase variations owing to differences in pumps' paths can be stabilized by using a fiber stretcher in one pump's path and monitoring one of the pumps' intensities at the TMF output. Since phase $\Delta\varphi$ is responsible for the direction of $\omega_{P1} + \omega_{P2} = \omega_{P3} + \omega_{P4}$ phase-sensitive parametric amplification process among the 4 pumps (where either one photon of pump 1 and one photon of pump 2 are annihilated, and one photon of pump 3 and one photon of pump 4 are created, or vice versa), controlling the fiber stretcher to lock either maximum or minimum gain for the observed pump wave will lock the relative phase $\Delta\varphi$.

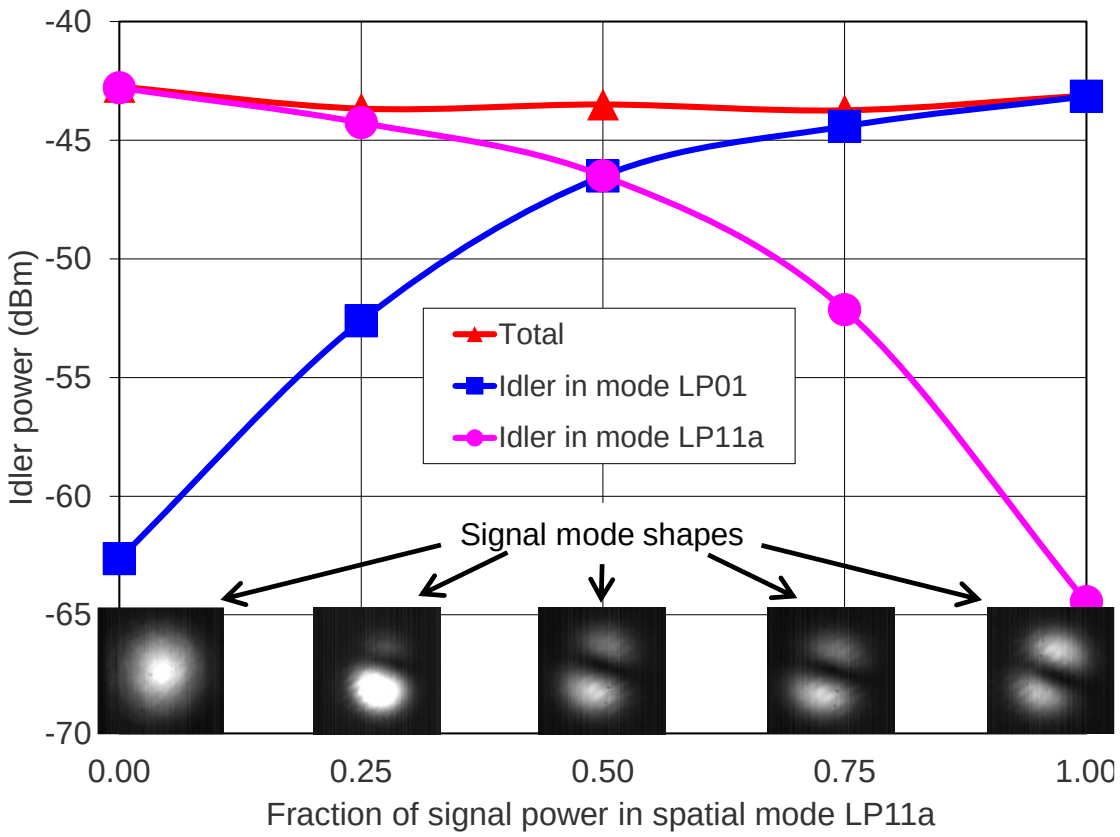

Figure 31. Idler powers for various signal mode superpositions.

3.2.4 Summary of generation of spatially-entangled photon-pair generation in a few-mode fiber

At first, we described a novel scheme for spatial-mode-entangled photon-pair generation in a few-mode fiber. We experimentally verified the underlying inter-modal parametric processes with two-mode classical signal input and demonstrated high mode purity of the generated idler. Then, using classical signal, we have simultaneously implemented the two inter-modal four-wave-mixing processes necessary for producing spatial-mode-entangled photon pairs in a few-mode fiber. We experimentally demonstrated generation of idler beam from a seed signal in a superposition of two fiber modes. For every signal mode superposition, we observe the indication of idler mode orthogonality to the signal mode. Thus, using a classical seed signal, we have

demonstrated that a combination of two inter-modal four-wave-mixing processes in a few-mode fiber can couple a signal in an arbitrary two-mode superposition to an idler in the orthogonal mode. While the scheme described in this part can lead to generation of spatial-mode entanglement in (LP_{01}, LP_{11a}) mode space of a few-mode fiber, an alternative few-mode-fiber-based scheme [36] may similarly result in generation of entanglement in optical angular momentum space, which we will describe in the next section.

3.3 OAM-selective frequency conversion and OAM-entangled photon-pair generation in a three-mode fiber

In this section, we present OAM-selective frequency conversion and OAM-entangled photon-pair generation in a three-mode fiber in Chapters 3.3.1 and 3.3.2, respectively.

3.3.1 OAM-selective frequency conversion in a three-mode fiber

3.3.1.1 Principle of operation of OAM-selective frequency conversion in a three-mode fiber

Our scheme employs a combination of two IM-FWM processes illustrated in Figure 32a. We use an elliptical-core FMF [6] that supports three non-degenerate modes: LP_{01}, LP_{11a}, and LP_{11b}, to be referred to as three-mode fiber (TMF) below. In IM-FWM process 1, pumps 1 and 2 downconvert LP_{11a} signal to LP_{11b} output. In process 2, pumps 3 and 4 downconvert LP_{11b} signal to the same LP_{11b} output mode. With all 4 pumps present, a selected superposition (e.g., OAM) of signal LP_{11a} and LP_{11b} modes is downconverted, whereas the orthogonal mode superposition is left unperturbed. Selection of the mode superposition is done by choosing relative powers of the 2 pairs of pump waves (i.e., relative weights of processes 1 and 2) and pump phase difference $\Delta\varphi = (\varphi_{p1} - \varphi_{p2}) - (\varphi_{p3} - \varphi_{p4})$. For each process, the phase-matching condition [33] requires equal group

velocities at the average frequencies of the two waves present in each spatial mode. These average frequencies, converted to wavelengths, are shown by dashed lines in Figure 32a. Figure 32b shows measured relative inverse group velocities (RIGV) $1/v_g$ of LP_{01}, LP_{11a}, and LP_{11b} modes of our TMF. The LP_{11a} and LP_{11b} curves are approximately parallel to the LP_{01} curve and are horizontally shifted from it by ~24 nm ($\Delta\nu_1$ = 3 THz) and ~41 nm ($\Delta\nu_2$ = 5.1 THz), respectively. Thus, the phase matching is satisfied when the dashed lines in Fig. 1a are separated by 17 nm and 41 nm for processes 1 and 2, respectively. Energy conservation and phase matching put the following 4 constraints on the frequencies of the 6 involved waves: $\nu_{p2} - \nu_{p1} = \nu_{p4} - \nu_{p3} = \nu_s - \nu_{WC} = \Delta\nu_2 - \Delta\nu_1$ and $\nu_s = \nu_{p3} - \Delta\nu_1$, where ν_s (or ν_{p3}) and ν_{p1} (or ν_{p2}) can be chosen arbitrarily, and subscript "WC" stands for wavelength-converted output. In our experiment, we downconvert signal from 1583 nm to 1601.1 nm, using wavelengths 1558.3, 1541.1, 1560.1, and 1542.9 nm for pumps 1, 2, 3, and 4, respectively.

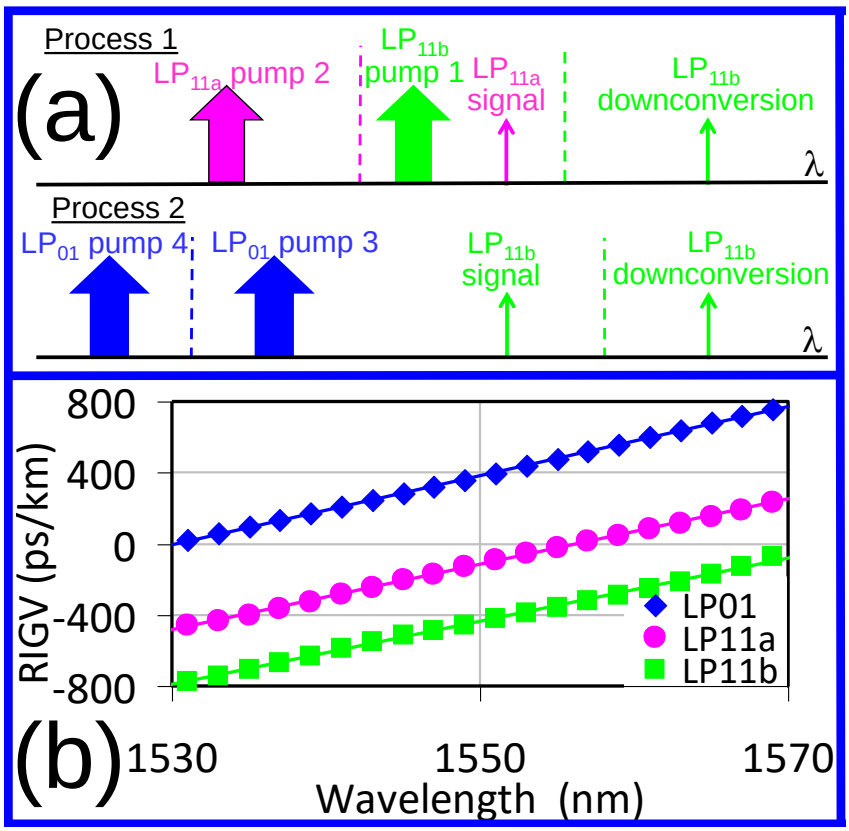

Figure 32. Two parametric processes, whose combination enables OAM-compatible mode-selective frequency conversion in the TMF. (b) Measured relative inverse group velocity (RIGV) data for the modes of our TMF.

3.3.1.2 Experimental setup

Figure 33 shows our experimental setup. All pumps and the signal are carved into 10-ns-long flat-top pulses with 10-MHz repetition rate by 3 intensity modulators. The pumps are then amplified by telecom-grade C-band erbium-doped fiber amplifiers (EDFAs). Pump 2 is converted to LP_{11a} mode by a phase plate PP1, combined with signal in free space by beam a dichroic beam splitter DBS, and combined with LP_{01}-mode pumps 3 and 4 by free-space beam splitter BS1. Pump 1 is converted to LP_{11b} mode by a phase plate PP2, combined these 4 beams by BS2, and coupled into the 1-km-long TMF by an objective. The TMF output is split between an infrared camera and a single-mode fiber (SMF) connected to the optical spectrum analyzer (OSA), which in this case measures the LP_{01} "output port" of the TMF. By inserting phase plate PP4 or PP5 prior to SMF

coupling, we can also measure LP_{11a} or LP_{11b} "output port" of the TMF. We can gradually vary the signal spatial mode from LP_{11a} to LP_{11b} by rotating the phase plate PP3 (when it is at 0°, it generates 100% LP_{11a} mode, and when it is at 90°, it generates 100% LP_{11b} mode; in the intermediate positions it generates various two-mode superpositions). To maximize IM-FWM, we co-polarize all three input waves in each process.

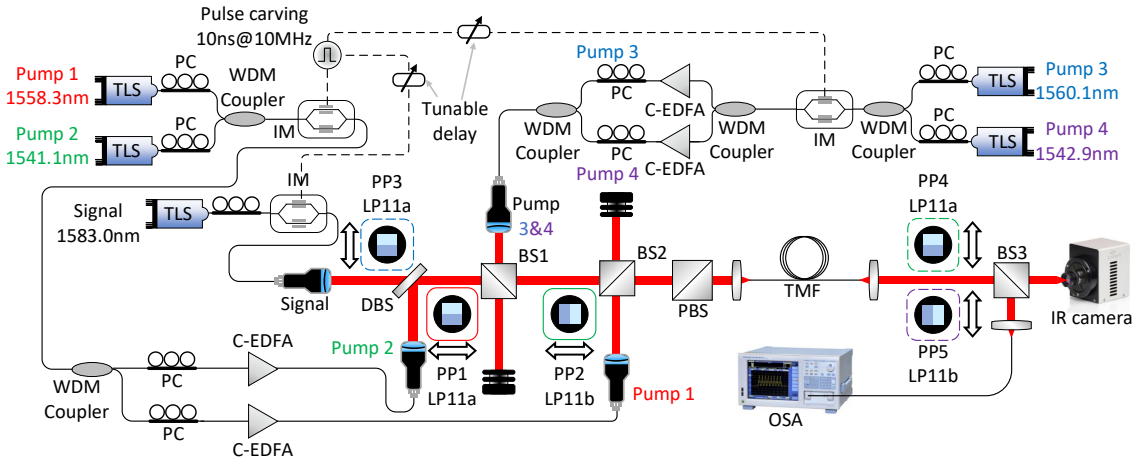

Figure 33. Experimental setup of two parametric processes, whose combination enables OAM-compatible mode-selective frequency conversion in the TMF.

3.3.1.3 Mode selectivity and conversion efficiencies with/without proper spatial mode of signal

Mode selectivity of each individual process is quantified by comparing conversion efficiency (CE) for the "desired" signal mode (LP_{11a} in process 1, LP_{11b} in process 2) to the CE for the "undesirable" signal mode (LP_{11b} in process 1, LP_{11a} in process 2). The blue and gray traces in Figure 34 show the ratio of these two efficiencies (crosstalk) for process 1 to be 21.2 dB.

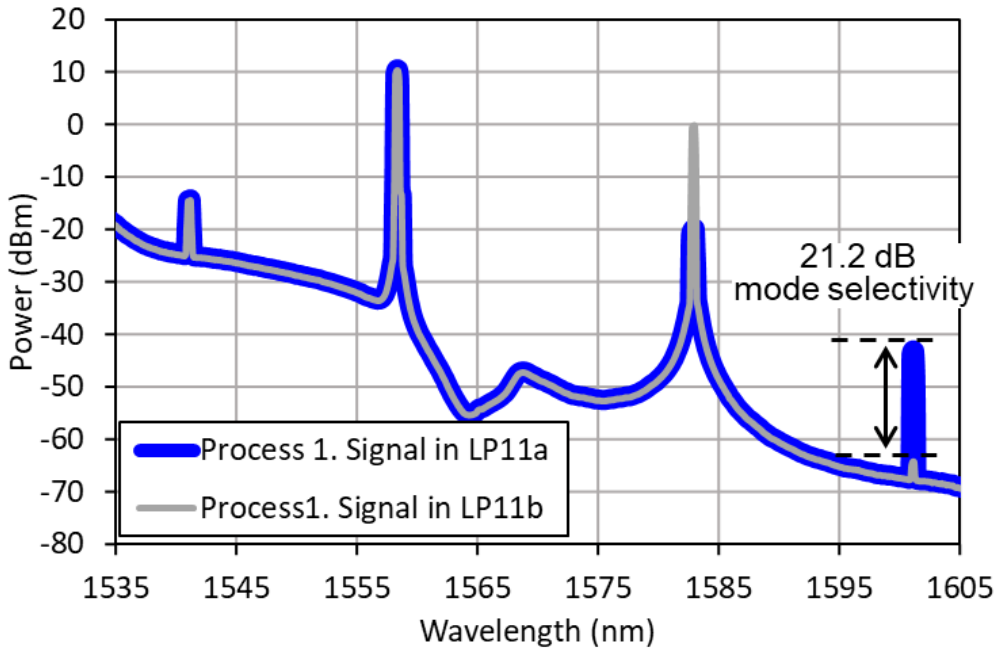

Figure 34. Optical spectra for process 1 with input signal in either LP_{11a} (thick blue) or LP_{11b} (thin gray) mode.

The gray and blue traces in Figure 35 show the ratio of these two efficiencies (crosstalk) for process 2 to be 23.7 dB. Figure 35 also shows the LP_{11b} output port spectrum for simultaneous processes 1 and 2 (4 pumps present). Average powers inside the TMF are 0 dBm for the signal and 10.5, 5.5, 9, and 7 dBm for pumps 1, 2, 3, and 4, respectively. At these powers the CEs for processes 1 and 2 are nearly equal.

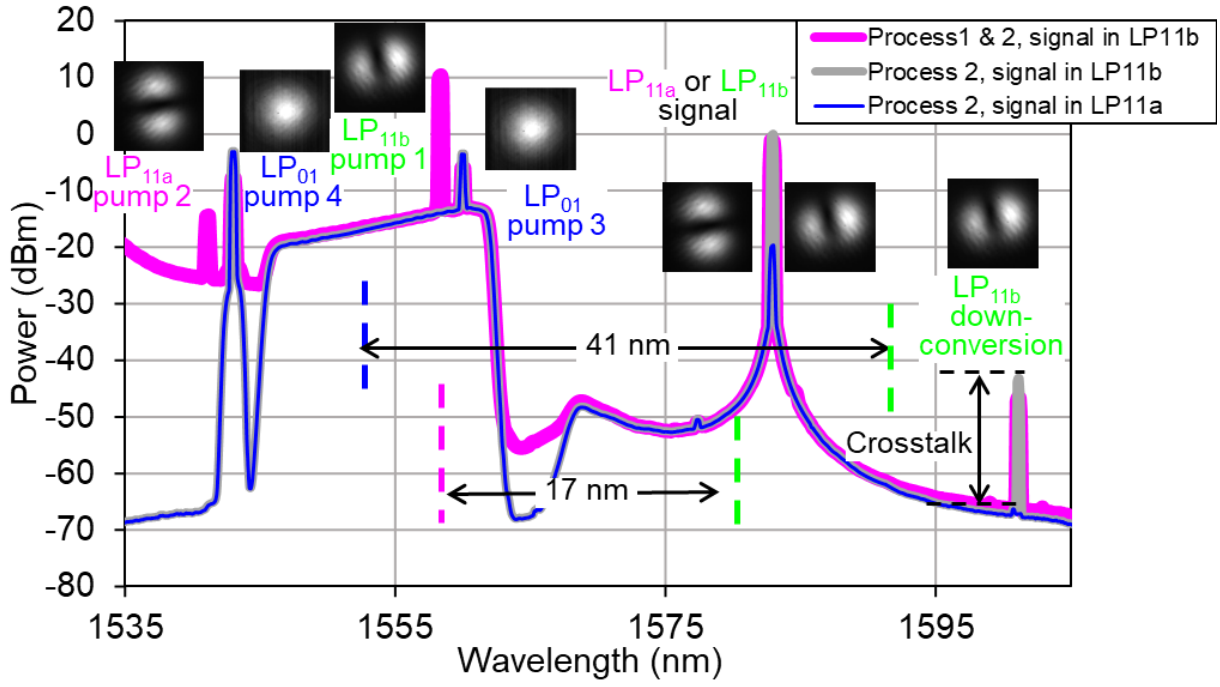

Figure 35. Spectra at LP_{11b} port for process 2 alone (gray, blue) and processes 1, 2 combined (purple).

If we had stable phase $\Delta\varphi = (\varphi_{p1} - \varphi_{p2}) - (\varphi_{p3} - \varphi_{p4})$, we would have been able to select for wavelength conversion a superposition of LP_{11a} and LP_{11b} modes with a specific relative phase (e.g., $\Delta\varphi = \mp\pi/2$ selects mode with OAM $l = \pm 1$). However, such stabilization (based on optical comb) has not been implemented in our setup yet, and our $\Delta\varphi$ fluctuates randomly on 0.1–1 μs scale. This means that we can observe mode-independent signal conversion to LP_{11b}, as both LP_{11a} and LP_{11b} components of any signal superposition are independently converted to LP_{11b} and added incoherently. This is illustrated in Figure 36, which shows nearly the same CEs (within 0.8 dB range from one another), measured for various signal superpositions with weight of LP_{11b} component ranging from 0 to 100%.

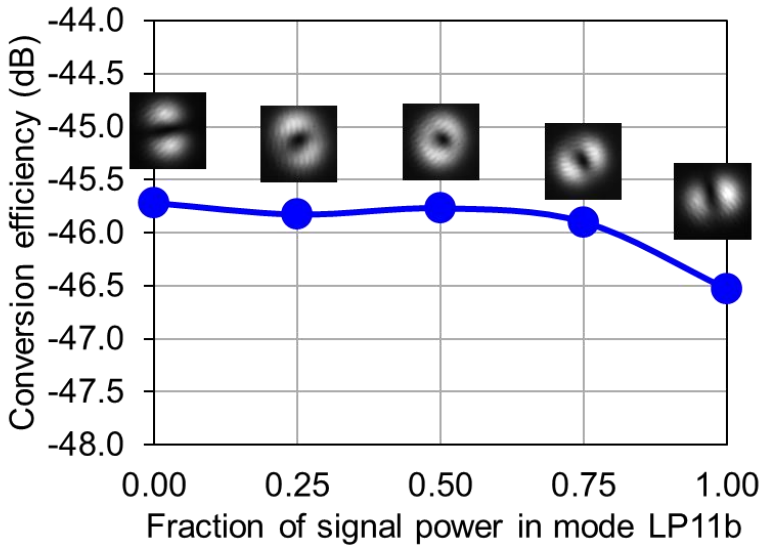

Figure 36. Conversion efficiency for various signal mode superpositions.

3.3.1.4 Summary

In this experiment, we described OAM-compatible mode-selective frequency conversion in a few-mode fiber and experimentally demonstrated downconversion of various superpositions of signal modes LP_{11a} and LP_{11b} to the same LP_{11b} mode with conversion efficiency differences <0.8 dB. We have simultaneously implemented two IM-FWM processes necessary for OAM-compatible mode-selective frequency conversion. We have shown that, in the absence of pump phase stabilization, this scheme produces mode-independent signal frequency conversion in LP_{11a}, LP_{11b} mode space. To increase CEs, one could employ high-power EDFAs and, possibly, a customized highly-nonlinear FMF with a reduced core size.

3.3.2 OAM-entangled photon-pair generation in a three-mode fiber

3.3.2.1 Principle of operation of OAM-entangled photon-pair generation in a three-mode fiber

Our spatial-mode entanglement scheme employs a combination of two IM-FWM processes of Figure 37a. We use an elliptical-core FMF [6], to be referred to as three-mode fiber (TMF) below, which supports three non-degenerate modes: LP_{01}, LP_{11a}, and LP_{11b}. In IM-FWM process 1, with the help of pumps 1 and 2 a signal photon is created in mode LP_{11a} at frequency ν_s, while idler photon is created in mode LP_{11b} at frequency ν_i. In process 2, their roles interchange: in the presence of pumps 3 and 4, signal photon at frequency ν_s is created in mode LP_{11b}, whereas the idler photon at frequency ν_i is created in mode LP_{11a}. With all four pumps present, processes 1 and 2 take place simultaneously. Their probabilities can be equalized by adjusting relative powers of the two pump pairs, which results in generation of the maximally-entangled state $|LP_{11b}\rangle_s|LP_{11a}\rangle_i + e^{i\varphi}|LP_{11a}\rangle_s|LP_{11b}\rangle_i$, where phase φ can be changed by varying the pump phase difference $\Delta\varphi = (\varphi_{p1} + \varphi_{p2}) - (\varphi_{p3} + \varphi_{p4})$. For $\varphi = \pi$ this state is equivalent to the OAM-entangled state $|l = +1\rangle_s|\ l = -1\rangle_i - |\ l = -1\rangle_s|\ l = +1\rangle_i$, where l is the orbital quantum number. For each of the two processes in Fig. 1a, the phase-matching condition [8] requires equal group velocities at the average frequencies of the two waves present in each spatial mode. These average frequencies, converted to wavelengths, are shown by dashed lines in Figure 37a. Figure 37b shows measured relative inverse group velocities (RIGV) $1/v_g$ of LP_{01}, LP_{11a}, and LP_{11b} modes of our TMF. The LP_{11b} curve is approximately parallel to the LP_{11a} curve and horizontally shifted from it by ~17 nm ($\Delta\nu_1$ = 2.1 THz), i.e., the phase matching is satisfied when the dashed lines in Fig. 1a are separated by 17 nm. Energy conservation and momentum conservation (phase matching) impose 4 constraints on the frequencies of the 6 involved waves: $\nu_{p1(p3)} = \nu_{i(s)} + \Delta\nu_1$ and $\nu_{p2(p4)} = \nu_{s(i)} - \Delta\nu_1$, hence any two

frequencies that are not separated by $\Delta\nu_1$ can be arbitrarily chosen. In our experiment, we choose signal to be at 1564.8 nm and idler to be at 1558.4 nm, which results in pumps 1, 2, 3, and 4 placed at 1541.3, 1582.4, 1547.3, and 1576.1, respectively.

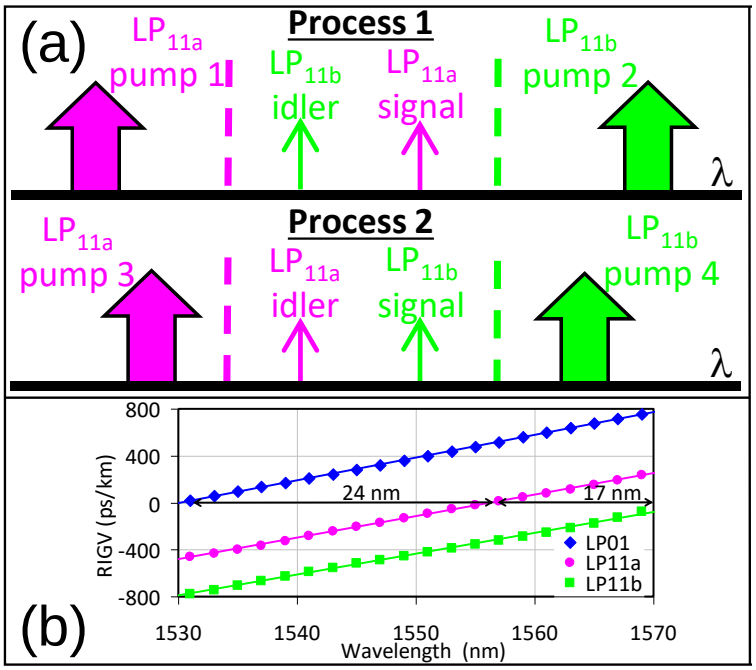

Figure 37. (a) Two parametric processes, whose combination enables generation of orbital-angular-momentum-entangled signal-idler photon pairs in the TMF. (b) Measured relative inverse group velocity (RIGV) data for the modes of our TMF.

3.3.2.2 Experimental setup

Our experimental setup is shown in Figure 38. The test signal and pumps are carved into 10-ns-long flat-top pulses with a 10-MHz repetition rate by intensity modulators and are amplified by telecom-grade C- and L-band erbium-doped fiber amplifiers (EDFAs). In process 1, signal and pump 1 are collimated and combined by a beam splitter BS in free-space. Their spatial modes are individually converted to LP_{11a} by two corresponding phase plates PP1 and PP2. Pump 2 is collimated into free space, converted to LP_{11b} mode by a phase plate PP3, and combined with signal and pump 1 via a dichroic beam splitter DBS. The three waves are then coupled into a 1-km-long TMF by an objective. The TMF output is collimated by a second objective. Part of the

output is observed on an infrared camera, and the remainder is coupled into a single-mode fiber (SMF) connected to the optical spectrum analyzer (OSA), which in this case measures the LP_{01} "output port" of the TMF. By inserting phase plate PP4 prior to SMF coupling, we can also measure LP_{11a} and LP_{11b} "output ports" of the TMF. In process 2, pump 1 and pump 2 are replaced by pump 3 and pump 4, respectively, by an optical switch (OS). For this process, signal is changed to LP_{11b} mode by PP1. In future experiments, the OS will be replaced by wavelength multiplexers to enable simultaneous presence of all 4 pumps. To maximize IM-FWM, we co-polarize all three input waves entering the TMF.

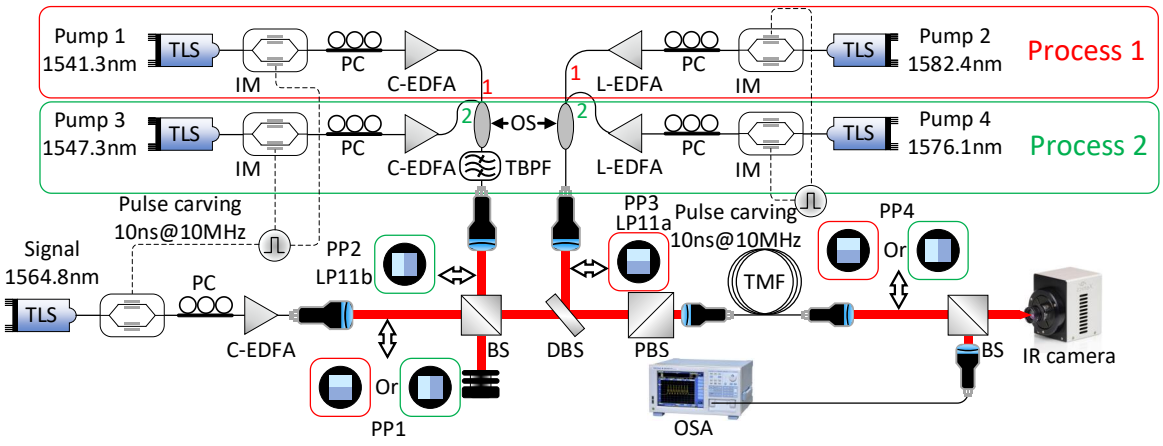

Figure 38. Experimental setup of two parametric processes, whose combination enables generation of orbital-angular-momentum-entangled signal-idler photon pairs in the TMF.

3.3.2.3 Mode purity and conversion efficiencies with/without proper spatial mode of signal

We characterize idler-mode impurity by comparing idlers in LP_{11a} and LP_{11b} output ports of the TMF. The depth of suppression of undesirable parametric interactions, i.e., mode selectivity of the parametric amplification processes 1 and 2, is quantified by comparing the idler generated by the desired process to that generated by an undesirable process, observed when the input signal is injected into a wrong mode: LP_{11b} for process 1, LP_{11a} for process 2.

Figure 39 and 40 show the spectra at the LP_{11a} (blue traces) and LP_{11b} (magenta traces) output ports of the TMF for processes 1 and 2, respectively. One can easily see a significant change in the idler power between the two traces, indicating high spatial-mode purity of the idler (18.1 and 18.7 dB for processes 1 and 2, respectively). Average powers inside the TMF are 0 dBm for the signal in all cases and 15, 9.5, 17, and 7.5 dBm for pumps 1, 2, 3, and 4, respectively. Easily-measurable signal-to-idler conversion efficiency is given by CE = $g - 1 = \langle n \rangle$, where g is the phase-insensitive parametric gain, and $\langle n \rangle$ is the average number of generated parametric photons per mode, also representing the probability of a single pair generation for our case of CE << 1. In Figure 39 and Figure 40, CEs are –46.1 and –47.1 dB for processes 1 and 2, respectively. The CEs of the undesirable processes, measured by injecting the signal into the wrong mode, are suppressed by more than 20 and 18.4 dB, compared to processes 1 and 2, respectively.

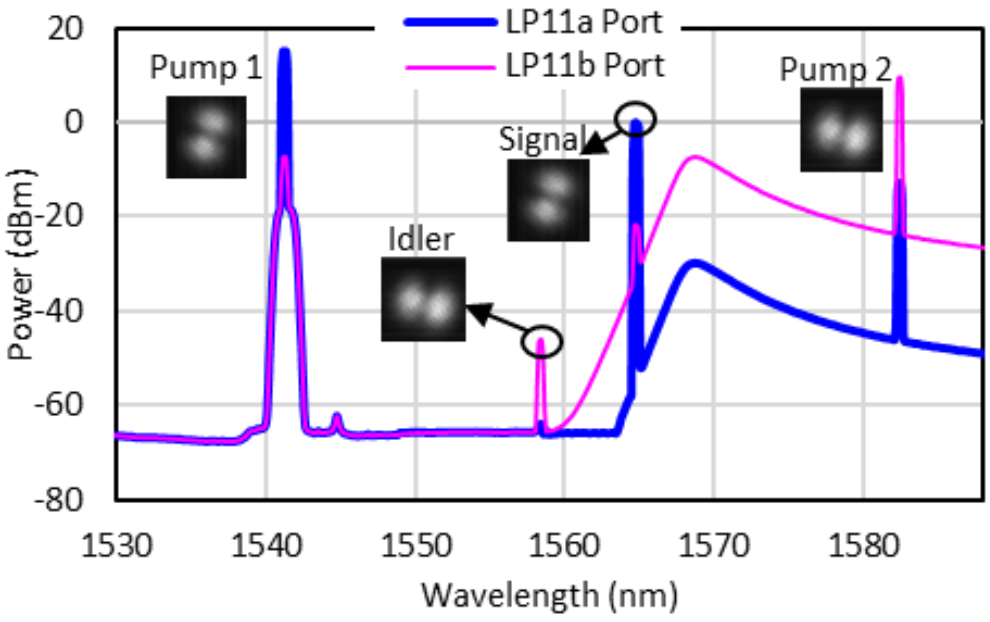

Figure 39. Optical spectra measured at the LP_{11a} (blue traces) and LP_{11b} (purple traces) output ports of the TMF for processes 1 when signal is in LP_{11a} mode.

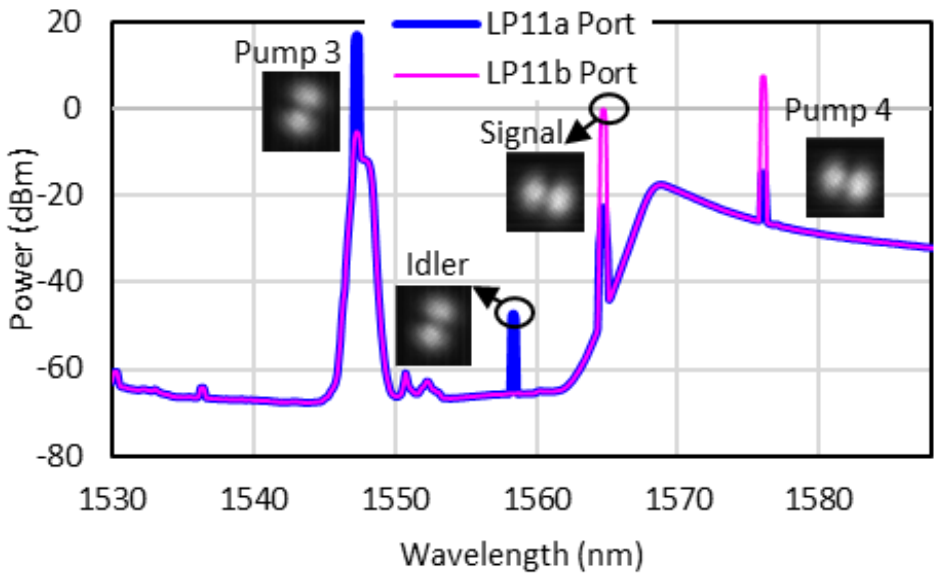

Figure 40. Optical spectra measured at the LP_{11a} (blue traces) and LP_{11b} (purple traces) output ports of the TMF for processes 2 when signal is in LP_{11b} mode.

3.3.3 Summary of OAM-selective frequency conversion and OAM-entangled photon pairs in a three-mode fiber

At first, we described a novel scheme for OAM-selective frequency conversion in a three-mode fiber. We showed OAM-compatible mode-selective frequency conversion in a TMF and experimentally demonstrated downconversion of various OAM-compatible superpositions of signal modes LP_{11a} and LP_{11b} to the same LP_{11b} mode with conversion efficiency differences <0.8 dB. We have also shown that, in the absence of pump phase stabilization, this scheme produces mode-independent signal frequency conversion in LP_{11a}, LP_{11b} mode space. In the next experiment, we used classical signal to experimentally verify mode-selective properties of the novel scheme for generation of OAM-entangled pairs, in which low-gain parametric amplifier in TMF couples LP_{11a} signal to LP_{11b} idler and LP_{11b} signal to LP_{11a} idler. In the spontaneous regime, the combination of these two processes would generate OAM-entangled signal-idler photon pairs.

Chapter 4: Conclusion

In this dissertation, we have simultaneously implemented two inter-modal four-wave mixing (IM-FWM) processes in a few-mode fiber, which are necessary for mode-selective frequency conversion, and experimentally demonstrated upconversion of a combination of two signal modes in (LP_{01}, LP_{11a}) mode space from C-band to fundamental mode in S-band with crosstalk below –20 dB. We observe mode-independent signal upconversion to LP_{01}, as both LP_{01} and LP_{11a} components of any signal superposition are independently upconverted to LP_{01} and added incoherently. Nearly the same CEs of –43.5 (within 1 dB range from one another) are measured for various signal superpositions with weight of LP_{11a} component ranging from 0 to 100%. CE for the undesirable signal mode is > 20 dB lower than the desired-mode's CE. Output mode has purity factor of 15.2 dB. To increase CEs, one could employ high-power EDFAs and, possibly, a customized highly-nonlinear FMF with a reduced core size. Mode-selective upconversion of arbitrary superpositions of LP_{01} and LP_{11a} can be achieved after stabilizing relative pump phases.

In effort to generate spatially-entangled photon pairs, we have demonstrated that a combination of two IM-FWM processes can couple arbitrary two-mode signal combination to an orthogonal idler mode. We combined both processes and observed that they couple the input two-mode seed signal to an orthogonal two-mode idler for various signal-mode superpositions. Nearly the same CEs of -43.5 (within 1 dB range from one another) have been measured for various signal superpositions with weight of LP_{11a} component ranging from 0 to 100%. CE for the undesirable signal mode is > 19 dB lower than the desired-mode's CE (orthogonal photon-pair crosstalk). To generate spatially-entangled photon pairs, we would further need to stabilize pump phases and to

perform narrow-band filtering of the pumps and idler beams to eliminate parasitic contribution of Raman scattering.

Also, OAM-selective frequency conversion and OAM-entangled photon pairs in a three-mode fiber (TMF) have been investigated, where we described a novel schemes for OAM-selective frequency conversion and OAM-entangled photon-pair generation in a TMF. We showed OAM-compatible mode-selective frequency conversion in a TMF and experimentally demonstrated downconversion of various superpositions of signal modes LP_{11a} and LP_{11b} to the same LP_{11b} mode with conversion efficiency differences < 0.8 dB. We also used classical signal to experimentally verify mode-selective properties of the novel scheme for generation of OAM-entangled pairs, in which low-gain parametric amplifier in TMF couples LP_{11a} signal to LP_{11b} idler and LP_{11b} signal to LP_{11a} idler.

Appendix I

List of Publications:

[1] Afshin Shamsshooli *et al*. "Reconfigurable spatial-mode-selective frequency conversion in a three-mode fiber", to appear in **Photonic Technology Letter, 2021**.

[2] Afshin Shamsshooli *et al*. "Progress Toward Spatially-Entangled Photon-Pair Generation in a Few-Mode Fiber", **Photonic Technology Letter, 2021, under review**.

[3] Afshin Shamsshooli *et al*. "Toward OAM-selective frequency conversion in a three-mode fiber", **CLEO, 2021, Accepted**.

[4] Afshin Shamsshooli *et al*. "Reconfigurable mode-selective frequency conversion in a three-mode fiber", IEEE Photon. Conf., 2020, paper ThF1.2.

[5] Afshin Shamsshooli *et al*. "Progress Toward Generation of Spatially-Entangled Photon Pairs in a Few-Mode Fiber", IEEE Photon. Conf., 2020, paper MI2.2.

[6] Afshin Shamsshooli *et al*. "Toward Generation of Orbital-Angular-Momentum-Entangled Photon Pairs in a Few-Mode Fiber", Frontiers in Optics / Laser Science Conference, September 14–17 2020, paper FM1D.2.

[7] Afshin Shamsshooli *et al*. "Mode-selective frequency conversion in a three-mode fiber", *CLEO 2020 conference*, San Jose, CA, May 15–20, 2020, paper SM3P.3.

[8] Afshin Shamsshooli *et al*. "Toward Generation of Spatially-Entangled Photon Pairs in a Few-Mode Fiber", *CLEO 2020 conference*, San Jose, CA, May 15–20, 2020, paper JTh2A.29.

[9] Guo, C., **Shamsshooli, A**., Vasilyev, M., Akasaka, Y., & Ikeuchi, T. “Noise figure study for a 3-stage hybrid amplifier using parametric wavelength converters and EDFA”, accepted to **Photonic Technology Letter, 2021**.

[10] Afshin Shamsshooli *et al*. “Noise figure of a 3-stage hybrid amplifier using parametric wavelength converters and EDFA”, IEEE Photon. Conf., 2020, paper WE3.4.

[11] Afshin Shamsshooli *et al*. "Multi-species gas analysis platform arrays for civil applications“, *ASCE Symposium*, South Padre Island, Texas, 2019.

[12] Afshin Shamsshooli *et al*. “Adaptive-optical-comb-enabled integrated multi-species gas analysis platform,” *College of Engineering Innovation Day*, University of Texas at Arlington, 2018 (3rd prize in student research competition).

[13] Afshin Shamsshooli *et al*. “Toward a Multi-Species Gas Sensor on a Chip,” *Frontiers in Optics / Laser Science conference*, Washington, DC, September 17–21, 2017, paper FTu4E.2.

References:

[1] D. J. , J. M. Fini, and Lynn E. Nelson, “Space-division multiplexing in optical fibres,” Nature Photon., vol. 7, no. 5, pp. 354-362, May 2013.

[2] Y. Weng, X. He, and Z. Pan, “Space division multiplexing optical communication using few-mode fibers,” Opt. Fiber Technol., vol. 36, pp. 155–180, Jul. 2017.

[3] Manurkar, Paritosh, Nitin Jain, Michael Silver, Yu-Ping Huang, Carsten Langrock, Martin M. Fejer, Prem Kumar, and Gregory S. Kanter. "Multidimensional mode-separable frequency conversion for high-speed quantum communication." Optica 3, no. 12 (2016): 1300-1307.

[4] Y. B. Kwon, M. Giribabu, L. Li, S. C. Samudrala, C. Langrock, M. Fejer, and M. Vasilyev, “Experimental demonstration of spatial-mode-selective frequency up-conversion in a multimode $\chi(2)$ waveguide,” in Proc. CLEO conference, San Jose, CA, June 5–10, 2016, paper STh3P.4.

[5] Y. B. Kwon, M. Giribabu, L. Li, C. Langrock, M. Fejer, and M. Vasilyev, “Single-photon-level spatial-mode-selective frequency up-conversion in a multimode $\chi(2)$ waveguide,” in Proc. CLEO conference, San Jose, CA, May 14–19, 2017, paper FF2E.1.

[6] F. Parmigiani, P. Horak, Y. Jung, L. Grüner-Nielsen, T. Geisler, P. Petropoulos, and D. Richardson, “All-optical mode and wavelength converter based on parametric processes in a three-mode fiber,” Opt. Express, vol. 25, no. 26, pp. 33602–33609, Dec. 2017.

[7] O. F. Anjum, P. Horak, Y. Jung, M. Suzuki, Y. Yamamoto, T. Hasegawa, P. Petropoulos, D. J. Richardson, and F. Parmigiani, “Broadband study of inter-modal Bragg scattering four wave mixing in multi-mode fibres,” in Proc. European Conference on Optical Communication, Rome, Italy, Sep. 23–27, 2018, pp. 1–3, doi: 10.1109/ECOC.2018.8535446.

[8] E. Nazemosadat, A. Lorences-Riesgo, M. Karlsson, and P. A. Andrekson, “Design of highly nonlinear few-mode fiber for C-band optical parametric amplification,” J. Lightwave Technol., vol. 35, no. 14, pp. 2810–2817, May 2017.

[9] O. F.Anjum, M. Guasoni, P. Horak, Y. Jung, P. Petropoulos, D. J. Richardson, and F. Parmigiani, “Polarization-insensitive four-wave-mixing-based wavelength conversion in few-mode optical fibers,” J. Lightwave Technol., vol. 36, no. 17, pp. 3678–3683, Sep. 2018[10] O. F. Anjum , M. Guasoni, P. Horak , Y. Jung, M. Suzuki, T. Hasegawa, K. Bottrill, D. J. Richardson, F. Parmigiani, and P. Petropoulos, “Selective wavelength conversion in a few-mode fiber,” Opt. Express, vol. 27, no. 17, pp. 24072–24081, Aug. 2019.

[11] G. Rademacher, R. Ryf, N. K. Fontaine, H. Chen, R. M. Jopson, R.-J. Essiambre, B. J. Puttnam, R. S. Luís, Y. Awaji, N. Wada, S. Gross, N. Riesen, M. Withford, Y. Sun, and R. Lingle, “Experimental investigation of parametric mode and wavelength conversion in a 4.7 km few-mode fiber,” in Proc. European Conference on Optical Communication, Rome, Italy, Sep. 23–27, 2018, pp. 1–3, doi: 10.1109/ECOC.2018.8535501.

[12] G. Rademacher, R. S. Luís, B. J. Puttnam, Y. Awaji, M. Suzuki, T. Hasegawa, and N. Wada, “Wide-band intermodal wavelength conversion in a dispersion engineered highly nonlinear FMF,” in Proc. Optical Fiber Communication conference, San Diego, CA, Mar. 3–7, 2019, paper W1C.4.

[13] G. Rademacher, R. S. Luís, B. J. Puttnam, H. Furukawa, R. Maruyama, K. Aikawa, Y. Awaji, and N. Wada, “Investigation of intermodal four-wave mixing for nonlinear signal processing in few-mode fibers,” IEEE Photon. Technol. Lett., vol. 30, no. 17, pp. 1527–1530, Sep. 2018.

[14] A. Mair, A. Vaziri, G. Weihs, and A. Zeilinger, “Entanglement of the orbital angular momentum states of photons,” Nature, vol. 412, no. 6844, pp. 313–316, Jul. 2001.

[15] A. Sit, F. Bouchard, R. Fickler, J. Gagnon-Bischoff, H. Larocque, K. Heshami, D. Elser, C. Peuntinger, K. Günthner, B. Heim, C. Marquardt, G. Leuchs, R. W. Boyd, and E. Karimi, "High-dimensional intracity quantum cryptography with structured photons," Optica, vol. 4, no. 9, pp. 1006–1010, Aug. 2017.

[16] W. Löffler, T. G. Euser, E. R. Eliel, M. Scharrer, P. St. J. Russell, and J. P. Woerdman, "Fiber transport of spatially entangled photons," Phys. Rev. Lett., vol. 106, no. 24, 240505, Jun. 2011.

[17] Y. Kang, J. Ko, S. M. Lee, S.-K. Choi, B. Y. Kim, and H. S. Park, "Measurement of the entanglement between photonic spatial modes in optical fibers," Phys. Rev. Lett., vol. 109, no. 2, 020502, 2012.

[18] N. H. Valencia, S. Goel, W. McCutcheon, H. Defienne, and M. Malik. "Unscrambling entanglement through a complex medium," Nature Phys., vol. 16, no. 11, pp. 1112–1116, Aug. 2020.

[19] H. Cao, S.-C. Gao, C. Zhang, J. Wang, D.-Y. He, B.-H. Liu, Z.-W. Zhou, Y.-J. Chen, Z.-H. Li, S.-Y. Yu, J. Romero, Y.-F. Huang, C.-F. Li, and G.-C. Guo, "Distribution of high-dimensional orbital angular momentum entanglement over a 1 km few-mode fiber," Optica, vol. 7, no. 3, pp. 232–237, Mar. 2020.

[20] D. Cozzolino, E. Polino, M. Valeri, G. Carvacho, D. Bacco, N. Spagnolo, L. K. Oxenløwe, and F. Sciarrino, "Air-core fiber distribution of hybrid vector vortex-polarization entangled states," Adv. Photon., vol. 1, no. 4, 046005, Aug. 2019.

[21] Rottwitt, Karsten, Jesper B. Christensen, Erik N. Christensen, and Jacob G. Koefoed. "Quantum information processing using intermodal four-wave mixing in multi-mode optical

fibers." In 2019 21st International Conference on Transparent Optical Networks (ICTON), pp. 1-3. IEEE, 2019.

[22] K. Rottwitt, J. G. Koefoed, and E. N. Christensen, “Photon-pair sources based on intermodal four-wave mixing in few-mode fibers,” Fibers, vol. 6, no. 2, 32, May 2018.

[23] C. Guo, J. Su, Z. Zhang, L. Cui, and X. Li, “Generation of telecom-band correlated photon pairs in different spatial modes using few-mode fibers,” Opt. Lett., vol. 44, no. 2, pp. 235–238, Jan. 2019.

[24] K. Sulimany and Y. Bromberg, “All-Fiber Source and Sorter for Multimode Correlated Photons,” preprint at arXiv:2012.14024 (2020).

[25] D. Cruz-Delgado, R. Ramirez-Alarcon, E. Ortiz-Ricardo, J. Monroy-Ruz, F. Dominguez-Serna, H. Cruz-Ramirez, K. Garay-Palmett, and A. B. U’Ren, “Fiber-based photon-pair source capable of hybrid entanglement in frequency and transverse mode, controllably scalable to higher dimensions,” Sci. Rep., vol. 6, 27377, Jun. 2016.

[26] R. W. Boyd, Nonlinear optics (Academic Press, 1992).

[27] G. P. Agrawal, Nonlinear Fiber Optics, 5th ed. (Academic Press, New York, 2012).

[28] Xiao, Y., Essiambre, R. J., Desgroseilliers, M., Tulino, A. M., Ryf, R., Mumtaz, S., & Agrawal, G. P. (2014). Theory of intermodal four-wave mixing with random linear mode coupling in few-mode fibers. Optics express, 22(26), 32039-32059.

[29] Su, Z., Zhu, X., & Sibbett, W. (1993). Conversion of femtosecond pulses from the 1.5-to the 1.3-μm region by self-phase-modulation-mediated four-wave mixing. JOSA B, 10(6), 1050-1053.

[30] Stolen, R. H., Bösch, M. A., & Lin, C. (1981). Phase matching in birefringent fibers. Optics letters, 6(5), 213-215.

[31] Demas, J., Steinvurzel, P., Tai, B., Rishoj, L., Chen, Y., & Ramachandran, S. (2015). Intermodal nonlinear mixing with Bessel beams in optical fiber. Optica, 2(1), 14-17.

[32] Stolen, R. H., Bjorkholm, J. E., & Ashkin, A. (1974). Phase-matched three-wave mixing in silica fiber optical waveguides. Applied Physics Letters, 24(7), 308-310.

[33] R.-J. Essiambre, M. A. Mestre, R. Ryf, A. H. Gnauck, R. W. Tkach, A. R. Chraplyvy, Y. Sun, X. Jiang, and R. Lingle, "Experimental investigation of inter-modal four-wave mixing in few-mode fibers," IEEE Photon. Technol. Lett., vol. 25, no. 6, pp. 539–542, Mar. 2013.

[34] P. G. Kwiat, E. Waks, A. G. White, I. Appelbaum, and P. H. Eberhard, "Ultra-bright source of polarization-entangled photons," Phys. Rev. A 60, R773–R776 (1999).

[35] A. Shamsshooli, C. Guo, F. Parmigiani, X. Li, and M. Vasilyev, "Toward Generation of Spatially-Entangled Photon Pairs in a Few-Mode Fiber," in Proc. CLEO conference, San Jose, CA, May 10–15, 2020, paper JTh2A.27.

[36] A. Shamsshooli, C. Guo, F. Parmigiani, X. Li, and M. Vasilyev, "Toward Generation of Orbital-Angular-Momentum-Entangled Photon Pairs in a Few-Mode Fiber," in Proc. Frontiers in Optics / Laser Science Conference, September 14–17, 2020, paper FM1D.2, doi: 10.1364/FIO.2020.FM1D.2.